# ARTICLE

# Axonal synapse sorting in medial entorhinal cortex

Helene Schmidt[1,2], Anjali Gour[1], Jakob Straehle[1], Kevin M. Boergens[1], Michael Brecht[2,3] & Moritz Helmstaedter[1]

**Research on neuronal connectivity in the cerebral cortex has focused on the existence and strength of synapses between neurons, and their location on the cell bodies and dendrites of postsynaptic neurons. The synaptic architecture of individual presynaptic axonal trees, however, remains largely unknown. Here we used dense reconstructions from three-dimensional electron microscopy in rats to study the synaptic organization of local presynaptic axons in layer 2 of the medial entorhinal cortex, the site of grid-like spatial representations. We observe path-length-dependent axonal synapse sorting, such that axons of excitatory neurons sequentially target inhibitory neurons followed by excitatory neurons. Connectivity analysis revealed a cellular feedforward inhibition circuit involving wide, myelinated inhibitory axons and dendritic synapse clustering. Simulations show that this high-precision circuit can control the propagation of synchronized activity in the medial entorhinal cortex, which is known for temporally precise discharges.**

Ultrastructural analysis of cortical synaptic connectivity by electron microscopy has typically been limited to small volumes of tens of micrometres in extent[1–7]. Similarly, connectivity analysis using multiple intracellular electrical recordings in brain slices is typically limited to testing small numbers of connections within an individual brain slice[8–15]. Only recently, larger-scale high-resolution three-dimensional imaging of neuronal circuits using electron microscopy has become feasible for volumes extending to several hundred micrometres for at least two dimensions[16–20], whereas this was previously unique to electrical recordings. These approaches allow the study of locally complete synaptic in- and output maps. Especially for mapping synapses along axons, the path length of the reconstructed axon is the key constraining factor, and this is limited by the smallest of the three imaged and reconstructed dimensions (40–52 μm in previous studies in the cortex[1,19,20], see ref. 21).

Here we used serial block-face scanning electron microscopy (SBEM[22]) and skeleton-based connectomic data analysis[23] to investigate the neuronal circuitry in layer 2 (L2) of the medial entorhinal cortex (MEC) of rats in three-dimensional electron microscopy datasets for which the smallest dimensions were 274 μm (juvenile, 25-day-old rat (P25)) and 101 μm (adult, 90-day-old rat (P90)). The second dataset was acquired and analysed after analysis of the first, yielding a reproducibility control of the results presented here.

Previous electrical recording studies of the MEC[14,15] have found that connectivity between excitatory neurons to is absent[14] or sparse[15], suggesting types of attractor models in the MEC that are based on purely inhibitory connectivity between excitatory neurons[14].

We find that at least 30% of the output synapses of excitatory neurons are made onto other excitatory targets. Notably, this excitatory connectivity had a peculiar distance dependence: when investigating the output synapses along the axons of excitatory neurons. we find that inhibitory neurons are targeted first, offset by about 120 μm along the path length of the axon to the innervation of excitatory neurons (path-length-dependent axonal synapse sorting (PLASS)). We furthermore find that axons frequently provide multiple closely spaced synapses on the same postsynaptic dendrites, further enhancing the ability of the excitatory neuron to activate the postsynaptic neurons at high temporal precision in a cellular feedforward inhibition (cFFI)

circuit. Our results reveal a level of synaptic specialization in the cerebral cortex that is beyond average cell-to-cell connectivity and emphasize the need for high-resolution connectomic circuit mapping. Using numerical simulations, we show that this circuit could enhance spike timing precision, and could control the propagation of synchronized activity.

## 3D electron microscopy and neuron reconstruction

We acquired and densely reconstructed two three-dimensional electron microscopy datasets: one with a size of $424 \times 429 \times 274\,\mu m^3$ from the MEC of a P25 male rat (Fig. 1a–c) with a voxel size of $11.24 \times 11.24 \times 30\,nm^3$ (increased to $11.24 \times 11.24 \times 50\,nm^3$ for the final 56 μm of the dataset) and one with a size of $183 \times 137 \times 158\,\mu m^3$ from the MEC of a P90 male rat (Extended Data Fig. 1a; note that the analysis of the P90 dataset was already performed when the 101-μm data in the third dimension had been acquired) with a voxel size of $11.24 \times 11.24 \times 30\,nm^3$ using SBEM[22]. For the acquisition of the large P25 dataset, the electron microscope was equipped with a custom-built microtome that we modified for continuous stage movement, which increased the effective acquisition speed to about 6 MVx s$^{-1}$ (Extended Data Fig. 1b–f, for details see Methods; the P90 dataset was acquired using conventional mosaic-based imaging). The tissue blocks were stained using enhanced en bloc staining[24] to provide high image contrast over the entire tissue block size. The tissue adjacent to the sample was stained for calbindin immunoreactivity (Extended Data Fig. 1g, h), confirming the location in the dorsal MEC and the relationship to the patches of pyramidal neurons in L2 of the MEC[25,26].

We then used our in-browser data annotation software webKnossos[27] for neurite reconstruction. In the P25 dataset, dendrites could be followed through the entire dataset, and axons could be followed through large parts of the image volume (see Methods). In the P90 dataset, dendrites and axons could be followed throughout (for calibration of traceability by multiple experts, see Methods). We first identified neuronal cell bodies in the datasets and asked a team of 24 student annotators to skeleton reconstruct the dendrites of all these neurons ($n = 665$ in P25, Fig. 1a–c; $n = 91$ in P90; total traced path length 2.89 m, average redundancy 2.0, that is, 1.45 m of unique neurites reconstructed within a total of 3,654 work hours using the orthogonal

[1]Department of Connectomics, Max Planck Institute for Brain Research, D-60438 Frankfurt, Germany. [2]Bernstein Center for Computational Neuroscience, Humboldt University, D-10115 Berlin, Germany. [3]NeuroCure Cluster of Excellence, Humboldt University, D-10115 Berlin, Germany.
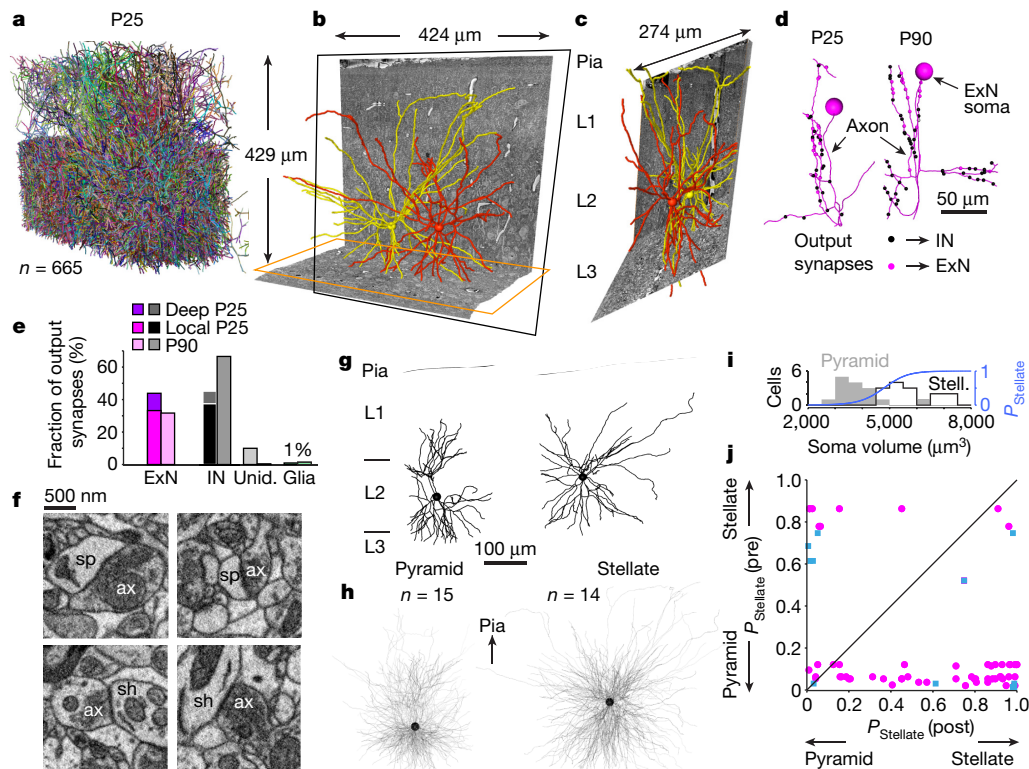
**Figure 1 | Electron-microscopy-based connectomic analysis in rat MEC. a–c,** In total, 665 neurons from cortical layers 2, 3 (L2, L3) were skeleton reconstructed[27] (**a**) to analyse the local circuitry within a three-dimensional electron microscopy dataset of MEC L2 of a P25 rat (**b, c**). **b, c,** Reconstruction of two example excitatory neurons in L2 (yellow, red) together with raw electron-microscopy data and dataset boundaries (dashed lines). **d,** Example reconstruction of somata and axons with all local output synapses targeting interneurons (INs, black) and ExNs (magenta) from the P25 dataset (left, see **a–c**) and for an additional three-dimensional electron microscopy dataset obtained from a 90-day-old rat (P90, right; Extended Data Fig. 1). **e,** Target distribution of output synapses ($n = 310$ for P25, $n = 284$ for P90) of ExNs ($n = 15$ for P25, $n = 7$ for P90). local, local target; deep, dendrite from deep layers; unid., unaccounted spines for which the continuation to the target dendrite was not uniquely identifiable (P25); glia, glial targets. **f,** Example electron microscopy micrographs of excitatory synapses made from presynaptic axons (ax) onto spines (sp., top) and shafts (sh, bottom), for criteria of synapse identification in SBEM, see ref. 32. **g,** Classification of ExNs into pyramidal neurons (left) and stellate cells (right) based on dendritic morphology. **h,** Superposition of soma and dendrites of pyramidal (left, $n = 15$) and stellate (right, $n = 14$) neurons for which expert consensus of the classification of the cell type was reached (Extended Data Fig. 2). **i,** Distribution of soma volume for consensus-classified pyramidal (grey) and stellate cells (black) in **h** and the resulting likelihood to encounter a stellate cell given the soma volume ($P_{stellate}$, blue). **j,** Map of synaptically connected ExN–ExN cell pairs (circles, P25; squares, P90) and the respective $P_{stellate}$ (pre, presynaptic; post, postsynaptic). Scale bars, 50 μm (**d**), 500 nm (**f**) and 100 μm (**g, h**).

tracing mode in webKnossos[27]). We first identified 22 excitatory neurons (ExNs, 15 in P25 and 7 in P90), for which we reconstructed their local axons (examples in Fig. 1d), yielding an average axonal path length per neuron of 555.4 μm (8.33 mm total) at P25 and 921.1 μm (6.44 mm total) at P90. Along these proximal axons, we identified all outgoing synapses ($n = 594$ (P25, $n = 310$; P90, $n = 284$), Fig. 1d–f), their postsynaptic targets, and matched these to the reconstructed neurons in the dataset. If the synaptic target was a dendrite that had not yet been traced, we added this dendrite to the reconstruction (113 and 135 additional dendrites at P25 and P90, respectively; dendrite classification was based on the rate of spines, calibrated to be >0.6 per μm for ExNs and <0.2 per μm for interneurons, see Methods). In the P25 dataset, 44% of these synapses were made onto ExNs and 45% onto interneurons. In the P90 dataset, 32% of synapses were made onto ExNs, 67% onto interneurons. To confirm that the synapse detection in SBEM data identified the expected range of synapse sizes, and is not biased towards larger synapses in particular, we measured the volume of a random subset of postsynaptic spines in our data ($0.13 \pm 0.12\,\mu m^3$, $n = 20$, P90 dataset), which is well within the range of values that have been reported so far[1,28]. It is noteworthy that studies using transmission electron microscopy appear to find smaller synapse sizes than those using scanning electron microscopy (compare data in refs 29–31 to refs 1, 28, 32 and this study; one methodological caveat may be the precise determination of cutting thickness for volume estimates).

To investigate how the connectivity between ExNs related to the at least two main types of excitatory neurons in the L2 of the MEC, namely pyramidal and stellate cells (Fig. 1g–i and Extended Data Fig. 2), we used previously proposed[15] morphological classification criteria and found that, in fact, the volume of the cell body was a strong predictor for the cell type ($n = 15$ pyramidal cells versus 14 stellate cells; volume $3,837 \pm 869\,\mu m^3$ versus $5,673 \pm 934\,\mu m^3$, mean $\pm$ s.d., $t$-test, $P < 10^{-5}$; Wilcoxon rank-sum test, $P < 10^{-4}$; Fig. 1i), yielding a 'stellate probability' $P_{stellate}$ based on soma size for each neuron. When analysing the ExN-to-ExN connectivity in relation to the likely cell type of the pre- and postsynaptic neurons, respectively (Fig. 1j), we find strongest evidence for connections from pyramidal to stellate cells ($n = 30$ out of 54 for $P_{stellate}(pre) < 0.25$ and $P_{stellate}(post) > 0.75$), and stellate to pyramidal cells ($n = 6$ out of 9 for $P_{stellate}(pre) > 0.75$ and $P_{stellate}(post) < 0.25$), and some examples of pyramidal-to-pyramidal ($n = 12$ of 54) and of stellate-to-stellate connections ($n = 2$ out of 9) (see refs 14, 15, 33).

## Path-length-dependent axonal synapse sorting

When we investigated the relationship between synapse position along the presynaptic excitatory axon and the type of synaptic target (Fig. 2), we found that synapses targeting interneurons were made first along the path of the axon, while synapses targeting excitatory neurons were made later. This was the case for excitatory neurons both in the P25
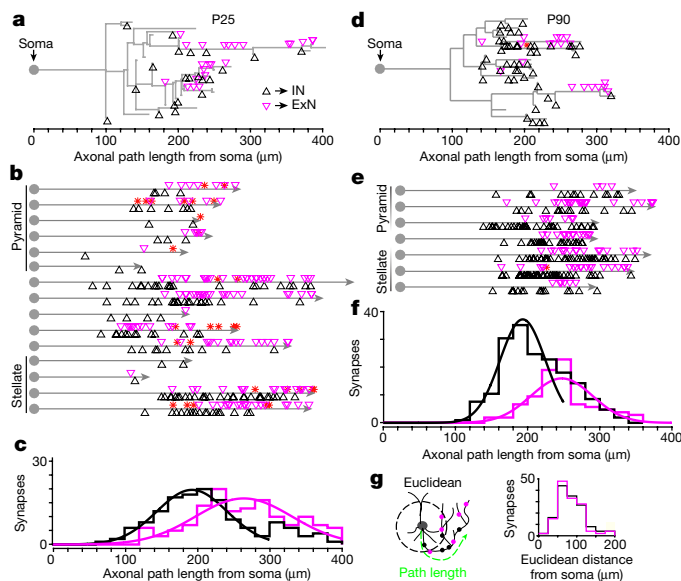
**Figure 2 | PLASS in rat MEC. a**, Example axonogram of one ExN with output synapses (triangles) onto interneurons (black) and ExNs (magenta) shown over length of the axonal path from the soma. **b**, **c**, The distribution of output synapses ($n = 307$) over the length of the axonal path to the soma (15 ExN axons, P25) shows a shift of inhibitory targets to more proximal locations along the axon ($n = 136$ (synapses onto excitatory cells) versus $n = 140$ (inhibitory targets)). Asterisk in **b** indicate unidentified synapses onto spine heads. Curves in **c** indicate Gaussian fits to the initial peaks of the distributions. See Fig. 6e for distance measurements in single axons and Extended Data Fig. 3a for cell-type specific analysis. **d–f**, Corresponding to **a–c** for the P90 dataset. Cells in **e** are sorted by increasing $P_{stellate}$ (top to bottom; see Fig. 1i and Extended Data Fig. 2). **g**, Summed distribution of output synapses along P25 ExN axons (as in **c**) analysed over the Euclidean (radial) distance to the ExN soma from which the axon originates. Note that the Euclidean distance distribution is indistinguishable for excitatory (magenta, $n = 136$) and inhibitory (black, $n = 140$) targets, indicating that synaptic sorting is specific to the axonal path length (**c**, **f**). See Extended Data Fig. 3b–f.

(Fig. 2a–c; $n = 15$ axons, $n = 136$ synapses onto excitatory cells versus $n = 140$ synapses onto inhibitory targets, $264 \pm 67\,\mu m$ versus $215 \pm 69\,\mu m$, mean $\pm$ s.d., $t$-test and Wilcoxon rank-sum test, $P < 10^{-8}$; randomization test, $P < 10^{-3}$; Fig. 2c) and P90 dataset (Fig. 2d–f; $n = 7$ axons, $n = 90$ synapses onto excitatory cells versus $n = 189$ synapses onto inhibitory targets, $247 \pm 43\,\mu m$ versus $210 \pm 45\,\mu m$, mean $\pm$ s.d., $t$-test and Wilcoxon rank-sum test, $P < 10^{-8}$; randomization test, $P < 10^{-3}$; Fig. 2f) and these results were found to be irrespective of the type of presynaptic excitatory neuron (Extended Data Fig. 3a).

We hypothesized that this unexpected axonal synaptic sorting could be related to an inhomogeneous availability of postsynaptic targets in the neuropil surrounding the presynaptic neurons. To test this hypothesis, we first analysed the distribution of output synapse targets when reported over their radial distance to the cell body of origin instead of their axonal path-length distance (Fig. 2g). This analysis showed that the radial distances of output synapses were indistinguishable for excitatory ($n = 136$) versus inhibitory ($n = 140$) targets ($82 \pm 34\,\mu m$ versus $85 \pm 34\,\mu m$; mean $\pm$ s.d., $t$-test, $P = 0.47$ and Wilcoxon rank-sum test, $P = 0.46$; Fig. 2g). Similarly, the positional bias of synapses was not explained by distance to the centres of the presumed modules in L2 of the MEC[25] (Extended Data Fig. 3b–d), nor fully accounted for by a shallow gradient of smooth dendrite density along the radial cortex axis (Extended Data Fig. 3e, f).

## Cellular feedforward inhibition

To understand the circuit context in which PLASS operates, we investigated the inhibitory neurons that receive input from the proximal output synapses of the excitatory axons (Fig. 3). Specifically, we wanted
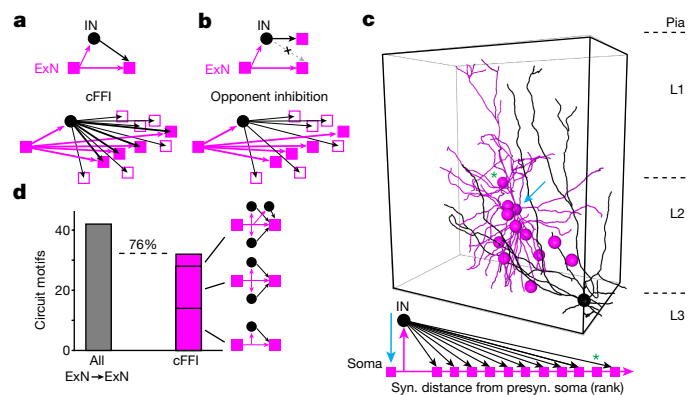


**Figure 3 | Possible configuration of the PLASS circuit. a**, **b**, Interneurons targeted by the more proximal synapses of ExN axons could either target the same ExNs (**a**, cFFI) or exclusively target a different population of ExNs from the source ExN targets (**b**, opponent or lateral inhibition). **c**, Example innervation of one presynaptic ExN (blue arrow; soma and dendrites are shown) that targets 11 other ExNs (magenta). Before targeting the ExNs, this ExN axon innervates an interneuron (black; soma and dendrites shown) that in turn innervates 10 out of the 11 ExN targets (the one exception is indicated by the asterisk), as proposed for cFFI. **d**, Frequency of cFFI circuit motifs in the local connectome (Supplementary Information 1, 2). cFFI motifs involving 1–3 interneurons are found in 76% (32 out of 42) of ExN–ExN connections. Opponent inhibition was refuted (see main text and Methods). See Extended Data Fig. 4 for functional comparison of pFFI versus cFFI circuits.

to know whether the PLASS-activated interneurons also target the same excitatory neurons that the source neuron targets (Fig. 3a)—or whether these interneurons would exclude the subset of excitatory neurons that were targeted by the excitatory source neuron (Fig. 3b). The latter would amount to an exclusive opponent or lateral inhibition, the former would constitute cFFI in the PLASS target circuit. Such a cFFI circuit has so far not been demonstrated in the cortex and could allow precise control of spike timing in the postsynaptic neuron (see below).

Figure 3c shows the soma and dendrite of one presynaptic ExN together with all of its 11 local excitatory target neurons and the PLASS-activated interneuron. In fact, 10 out of 11 of these targets were also innervated by that interneuron. In the entire population, 76% (32 out of 42) connections between excitatory neurons were matched by PLASS-activated interneuron innervation involving 1–3 interneurons (Fig. 3d; a total of $n = 54$ cFFI circuit motifs), showing a high prevalence of cFFI in MEC L2. Given that we may miss synaptic connectivity in three-dimensional electron microscopy imaging of limited volumes owing to incomplete axonal reconstructions, this data refutes an opponent inhibition model at $P < 10^{-7}$ under biological wiring noise of up to 30% (randomization test, see Methods). Even a random wiring model between interneurons and ExNs is refuted at $P < 10^{-3}$, yielding the cFFI model as the most likely explanation of our data.

We next investigated the potential functional significance of cFFI circuits. Feedforward inhibition has been described for several pathways in the mammalian brain, notably for the thalamocortical input to layer 4 (refs 34, 35), the mossy fibre input to cerebellar granule cells[36,37], and non-local input to pyramidal cells in the hippocampus (for example, refs 38, 39). In the latter circuit, feedforward inhibition was shown to enhance the precision of postsynaptic spike timing in CA1 pyramidal cells when activating the presynaptic excitatory axons[40]. However, in all of these previously described settings, the presynaptic neuronal population was activated by bulk electrical stimulation, such that it could not be determined whether presynaptic neurons activating the post-synaptic excitatory neuron were the same ones as those activating the interneurons, or whether they were from the same population, but not identical at the single-cell level (population feedforward inhibition (pFFI); Extended Data Fig. 4a). In the cerebellar circuit, recent data point to such a disjunct pFFI configuration[41]. By contrast, the cFFI
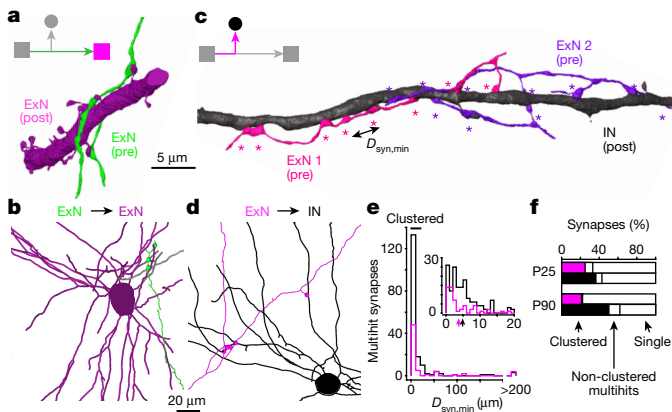
**Figure 4 | Dendritic synapse clustering in the MEC. a, b**, Examples of connections between ExNs (green, violet), in which synapses are spaced at a distance $D_{syn,min}$ of less than $20\,\mu m$ along the same postsynaptic dendrite (P25 dataset). **c, d**, Examples of connections between ExNs (magenta, violet) and interneurons (black) for the P90 dataset. Note that the interneuron dendrite is innervated by two ExN axons with $n = 10$ (violet) and $n = 8$ (magenta) clustered synapses (**c**). **e**, Minimal inter-synaptic distances $D_{syn,min}$ along the postsynaptic dendrite (see arrow in **c**) between synapses of the same presynaptic ExN axon for all connected cell pairs in the P25 and P90 datasets that involved multiple synapses per cell pair (multi-hit). Synapses with $D_{syn,min} < 20\,\mu m$ were considered clustered. Note that the large majority of these synapses has a minimal inter-synaptic distance $D_{syn,min}$ that is even less than $10\,\mu m$ (inset; arrows, mean, $3.7\,\mu m$ (onto ExNs) and $4.8\,\mu m$ (onto interneurons)). **f**, Fraction of synapses involved in multi-hit connections and clustered connections. Note that at least 12% of all ExN–ExN connections (magenta) and at least 24% of all ExN–interneuron connections (black) involve dendritic synapse clustering. Scale bars, $5\,\mu m$ (**a**, **c**) and $20\,\mu m$ (**b**, **d**).

configuration found here in the MEC (Fig. 3a and Extended Data Fig. 4c) implies that the same presynaptic neurons innervate both the postsynaptic ExN and the interneurons that provide feedforward inhibition.

We therefore studied whether this cFFI circuit could further enhance spike timing precision when compared to the pFFI circuit (Extended Data Fig. 4). We performed numerical simulations of an example circuit modelled after the estimated convergences in our circuit data (see Methods), comparing a pure pFFI configuration with a cFFI circuit such as the one we found in the MEC. In fact, the occurrence of action potentials in the postsynaptic ExN population was temporally more precise, and further suppressed in the cFFI circuit compared to the pFFI circuit (Extended Data Fig. 4e–j). Thus, cFFI can further enhance spike timing precision in local circuits of MEC L2 under conditions of transient, substantial population activity (50–90 Hz presynaptic activity; Extended Data Fig. 4j).

### Clustered postsynaptic innervation

Next we asked whether the precise synapse positioning along the excitatory axons might be matched by a positional preference of these synapses on the dendrites of target neurons. We found that the presynaptic excitatory axons target the postsynaptic excitatory dendrites (Fig. 4a, b; see also examples in ref. 1) as well as the postsynaptic inhibitory dendrites (Fig. 4c, d) with multiple closely spaced synapses. Quantified over all connections with more than one synapse (multi-hit; Fig. 4e, P25 and P90), 76% (185 out of 242) synapses were spaced at less than $10\,\mu m$ distance from each other, and 82% were spaced at less than $20\,\mu m$. Figure 4c shows an extreme example of two presynaptic excitatory axons that each make 8 and 10 synapses within about $52\,\mu m$ onto the postsynaptic interneuron dendrite. Clustered synapses were on average $3.7\,\mu m$ (onto ExNs) and $4.8\,\mu m$ (onto interneurons) apart (inset in Fig. 4e). When also considering synaptic connections with just one synaptic contact (Fig. 4f; note that the number of synapses in these
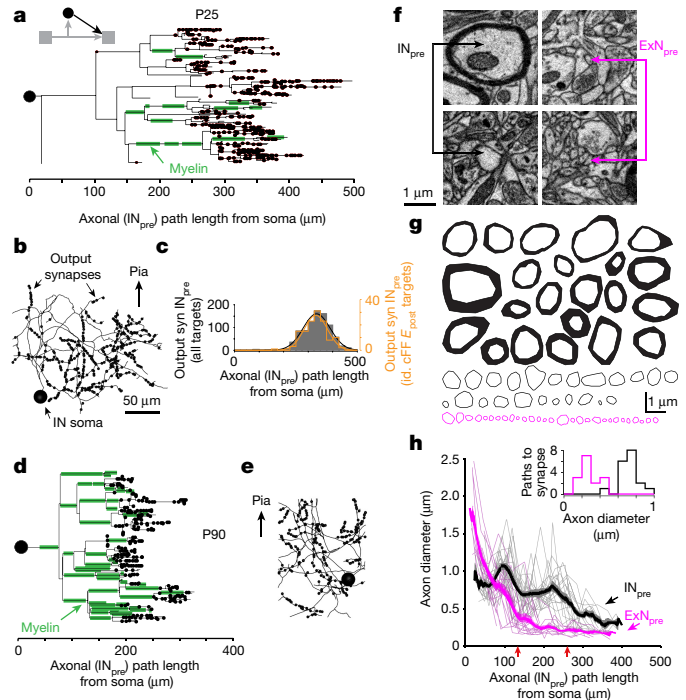


**Figure 5 | Axonal properties of interneurons involved in cFFI. a**, Axonogram of one interneuron (P25) with $n = 401$ output synapses. Note the stretches of myelinization before output synapses are established (green). **b**, Two-dimensional projection of the same axon (4.5 mm path length) with synapse positions. **c**, Distribution of interneuron output synapses along the length of the axonal path for 3 interneurons (Extended Data Fig. 5a) for all their output synapses ($n = 884$, black) and those synapses involved in the cFFI circuits ($n = 131$, orange). **d**, Axonogram of one interneuron ($n = 270$ synapses, P90) showing complete myelinization before synapses are established. **e**, Two-dimensional projection of the same axon with synapse positions (3.7 mm reconstructed axonal path length). **f**, Example cross-sections of interneuron (left) and ExN axons (right) showing substantial diameter differences. **g**, Overview of cross-section contours of interneuron axons (black, top; $n = 45$ sampled at $170\,\mu m$ from the soma of four interneurons; thickening indicates myelinization) and 29 cross-sections of ExN axons (magenta, bottom; $n = 29$ sampled at $170\,\mu m$ from the soma of six ExN). **h**, Change in the axon diameters (mean $\pm$ s.e.m. at intervals of $25\,\mu m$) along the trajectory between soma and distal synapses for three interneurons ($n = 18$ synapses, grey traces) and four ExNs ($n = 16$ synapses, magenta traces) (P25; P90 is shown in Extended Data Fig. 5b). Note the about 2.5-fold larger diameter of interneuron axons between about $130$–$260\,\mu m$ path length (red arrows). Inset, distribution of the mean axon diameter (over the interval between the red arrows) for 15 excitatory (magenta) and 18 inhibitory (black) axonal trajectories ($0.29 \pm 0.11\,\mu m$ versus $0.72 \pm 0.11\,\mu m$, mean $\pm$ s.d., $t$-test, $P < 10^{-11}$, Wilcoxon rank-sum test, $P < 10^{-5}$). Scale bars, $50\,\mu m$ (**b**, **e**) and $1\,\mu m$ (**f**, **g**).

connections is probably artificially reduced by axonal pruning based on three-dimensional sample size), dendritic clustering occurs in at least 18% of all single- and multi-hit connections (12% for excitatory and 24% for inhibitory targets). This is more frequent than previously reported for supragranular layers of the mouse primary visual cortex[20], where 9% of all excitatory connections were multi-hit connections (and an unreported fraction of these clustered; our multi-hit fraction was, in contrast to this study, 21%), and substantially more frequent than found in paired recording studies[9–12].

### Axonal properties of feedforward interneurons

Having found PLASS in the excitatory branch of the cFFI circuit (Fig. 3), we next investigated the inhibitory branch of this circuit. We first measured the path-length distribution of output synapses along the axons of interneurons (Fig. 5a–c; $n = 3$ interneurons P25; Extended

Data Fig. 5a); these axons showed no evidence for a positional bias of the cFFI synapses compared to all synapses ($n = 884$ interneuron synapses versus $n = 131$ cFFI synapses, $334 \pm 55\,\mu m$ versus $331 \pm 47\,\mu m$, mean $\pm$ s.d., $t$-test, $P > 0.5$; Fig. 5c). We noticed, however, that the interneuron axons were frequently myelinated before establishing the output synapses (Fig. 5a), with myelination of all axonal branches of a P90 interneuron (Fig. 5d, e). Furthermore, the diameter of the interneuron axons appeared very large compared to the axon diameter of the excitatory axons in the cFFI circuits (Fig. 5f). When quantifying cross-sectional diameters of inhibitory and excitatory axons (Fig. 5g, h), we find that the inhibitory axons show a 2.5-fold wider diameter along their path after the axon initial segment until the distance at which most output synapses are formed ($n = 15$ excitatory versus $n = 18$ inhibitory paths to synapse, $0.29 \pm 0.11\,\mu m$ versus $0.72 \pm 0.11\,\mu m$, mean $\pm$ s.d., $t$-test, $P < 10^{-11}$, Wilcoxon rank-sum test, $P < 10^{-5}$; Fig. 5h, Methods and Extended Data Fig. 5b). This was a remarkable finding: a recent study had reported strong myelination of interneuron axons in supra-granular layers of the primary visual cortex (ref. 42), but axon diameters of interneurons were not substantially larger than for the ExN axons in that study. Together, our finding of up to 100% myelinization and 2.5-fold wider axonal diameters in the inhibitory branch of the cFFI circuit could provide accelerated transmission of action potentials from the interneuron (IN) to its targets.

## PLASS and cFFI circuits

We next studied the subcellular arrangement of the converging inhibitory and excitatory synapses onto the postsynaptic excitatory neurons (Fig. 6a, b). In the cFFI circuits, we find that the imbalance of inhibitory synapses converging onto the postsynaptic neuron over the number of converging excitatory synapses is on average $N_{\mathrm{syn}}(\mathrm{IN})/N_{\mathrm{syn}}(\mathrm{ExN}) = 2.2 \pm 1.7$ ($n = 54$ cFFI circuits, mean $\pm$ s.d., right-tailed $t$-test against 1, $P < 10^{-5}$, Fig. 6c). Furthermore, the position of these synapses on the postsynaptic dendrites is biased such that excitatory inputs in the cFFI circuits are more distal than inhibitory inputs (Fig. 6b, d; $n = 54$ cFFI circuits, $75.3 \pm 35.8\,\mu m$ for ExN versus $45.4 \pm 18.2\,\mu m$ for interneuron synapses, mean $\pm$ s.d., paired $t$-test, $P < 10^{-6}$), allowing strong inhibition of excitatory inputs in the cFFI configuration.

The demonstration of PLASS (Fig. 3) had been an average offset of synapse positions lumped over many axons. Given the concrete cFFI circuits, we were now able to measure the PLASS distance for each of these cFFI circuits (Fig. 6e). This analysis showed that synapses onto excitatory neurons were on average $117.4 \pm 79.7\,\mu m$ more distally positioned along the presynaptic axon than those onto interneurons ($n = 54$ circuits, the mean path length of synapses was $269 \pm 57.5\,\mu m$ onto excitatory targets and $151.6 \pm 59.2\,\mu m$ onto inhibitory targets, mean $\pm$ s.d., paired $t$-test, $P < 10^{-17}$).

Finally, we explored possible functional implications of the precise subcellular arrangement of synapses in this cFFI circuit. We had found five main features: (1) PLASS in the excitatory axon (Figs 2, 6e; synapse offset of about $120\,\mu m$); (2) small-diameter ExN axons (Fig. 5f–h); (3) dendritic synapse clustering, especially onto interneuron dendrites (Fig. 4); (4) highly myelinated large-diameter interneuron axons (Fig. 5f–h); (5) an about twofold excess of interneuron synapses, positioned closer to the soma than ExN synapses on the cFFI target neurons (Fig. 6a–d). While each of these findings alone would make an interpretation in terms of the timing of propagation of action potentials unlikely (because the involved temporal delays were in the sub-millisecond range), the collective appearance of these mechanisms could possibly enable precisely timed inhibitory control of postsynaptic action potentials. To study this quantitatively, we performed numerical simulations of the cFFI circuit (Fig. 6f–i and Extended Data Fig. 6), implementing the additional subcellular findings (1–4) that are listed above (Fig. 6f). In particular, we varied the temporal delays that were possibly induced by PLASS (findings 1 and 2, summarized as $\Delta t_{\mathrm{PLASS}}$) and
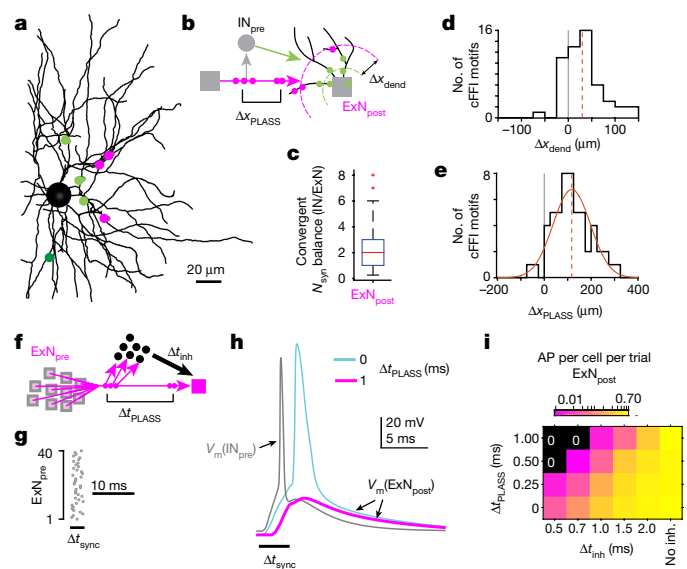


**Figure 6 | Convergence of the cFFI circuit and effects of PLASS on propagation of synchronous excitatory activity in the MEC. a,** Example reconstruction of a postsynaptic ExN (black) with cFFI synapse positions on the postsynaptic dendrites (coloured circles; from interneurons, green; from ExN, magenta). **b,** Sketch of the relevant geometric dimensions: postsynaptic dendritic synapse distance between ExN and interneuron inputs $\Delta x_{\mathrm{dend}}$; presynaptic axonal synapse offset due to PLASS ($\Delta x_{\mathrm{PLASS}}$), see **d, e. c,** Relative number of inhibitory versus excitatory synapses converging onto $E_{\mathrm{post}}$ in 54 cFFI circuits (on average $2.2 \pm 1.7$-fold excess of interneuron synapses, mean $\pm$ s.d.). **d,** Average offset of ExN synapses (more distal) and interneuron synapses (more proximal) on postsynaptic dendrites ($\Delta x_{\mathrm{dend}} = 30 \pm 40\,\mu m$, $n = 54$ cFFI circuits, dashed line). **e,** Average distance of synapses involved in cFFI along the presynaptic ExN axon ($\Delta x_{\mathrm{PLASS}}$). Excitatory synapses onto ExNs are $117.4 \pm 79.7\,\mu m$ (dashed) more distal than the corresponding synapses onto interneurons ($n = 54$ circuits). **f,** Sketch of cFFI circuit indicating delay of action potential conduction based on PLASS ($\Delta t_{\mathrm{PLASS}}$) and inhibitory delay combining action potential conduction time in the inhibitory axon and synaptic release ($\Delta t_{\mathrm{inh}}$). **g,** Example of simulated synchronous presynaptic population activity (1 action potential per neuron within $\Delta t_{\mathrm{sync}} = 3$ ms) in the PLASS–cFFI circuit (**f**). **h,** Example of simulated membrane potential transients following a synchronous presynaptic activation (**g**) in the interneuron (grey) and the postsynaptic ExN with (magenta) and without (cyan) PLASS-based presynaptic delay $\Delta t_{\mathrm{PLASS}}$. Note that for such synchronous presynaptic activity, the cFFI circuit alone cannot suppress the postsynaptic ExN to discharge an action potential, whereas cFFI with a PLASS-based delay of $\Delta t_{\mathrm{PLASS}} = 1$ ms can. **i,** Quantification of postsynaptic suppression of action potentials upon brief synchronized presynaptic population activity with a dependence on PLASS-based delay ($\Delta t_{\mathrm{PLASS}}$) and delay of inhibitory action potential conduction and synaptic release ($\Delta t_{\mathrm{inh}}$). Note that for a range of $\Delta t_{\mathrm{inh}} = 0.5$–$0.7$ ms and $\Delta t_{\mathrm{PLASS}} = 0.5$–$1$ ms, faithful suppression of postsynaptic discharge of action potentials is possible. See Extended Data Fig. 6 and Discussion. Scale bar, $20\,\mu m$ (**a**).

the conduction and synaptic transmission delays induced by the inhibitory axon (finding 4, $\Delta t_{\mathrm{inh}}$).

We speculated that precise millisecond timing might be critical in cases when the presynaptic population is active in tight synchrony. To emulate this, we activated the presynaptic excitatory neurons to discharge one action potential within 3 or 10 ms (Fig. 6g and Extended Data Fig. 6a) and investigated the postsynaptically converging postsynaptic potentials (PSPs) (Fig. 6h). Without PLASS ($\Delta t_{\mathrm{PLASS}} = 0$) the inhibitory PSPs arrived too late to influence the first action potential of the postsynaptic ExN. However, when adding PLASS that yielded a delay of $\Delta t_{\mathrm{PLASS}} = 1$ ms (corresponding to a conduction velocity of $120\,\mu m\,ms^{-1}$ in the ExN axon given the measured PLASS offset $\Delta x_{\mathrm{PLASS}}$; Fig. 6e), the inhibitory cFFI input arrived in time to completely

suppress the postsynaptic action potential (Fig. 6h, shown for inhibitory delay of $\Delta t_{inh} = 0.7$ ms). When screened over varying PLASS delays, $\Delta t_{PLASS}$, and inhibitory conduction delays, $\Delta t_{inh}$, we find that PLASS enables full suppression of action potentials after highly synchronous presynaptic activity for $\Delta t_{PLASS} \geq 0.5$ ms (with $\Delta t_{inh} = 0.5$ ms inhibitory delay) and $\Delta t_{PLASS} = 1$ ms with $\Delta t_{inh} = 0.7$ ms inhibitory delay. In addition, for $\Delta t_{inh} = 0.7$ ms and $\Delta t_{PLASS} = 0.5$ ms, postsynaptic activity is reduced about 200-fold (from 0.58 to 0.0025 spikes per cell per trial; Fig. 6i). In previous studies in the rat cortex, the latency between the peak of the action potential in local cortical interneurons and the onset of the inhibitory PSP in postsynaptic excitatory cells has been found to be between 0.5 and 1.1 ms (refs 43, 44). Given the strong myelination and wide diameter of the interneuron axons that we found in the MEC, it is therefore plausible that $\Delta t_{inh}$ is in a range (Fig. 6i) that enables the PLASS–cFFI circuit to modify or preempt the propagation of highly synchronous excitatory activity. Furthermore, the synchrony block was stable with additional background activity (Extended Data Fig. 6b, c), and activity propagation could be unblocked by an additional postsynaptic gating input (Extended Data Fig. 6d–h).

## Discussion

We discovered PLASS of output synapses along the axons of excitatory neurons in the rat MEC, a previously undescribed level of specificity in neuronal circuits of the mammalian cerebral cortex. We found that PLASS acts in a cFFI circuit, in which synapses are frequently clustered, in particular on the dendrites of postsynaptic interneurons. The inhibitory branch of the circuit appears to be shaped for fast transmission of action potentials using myelinated, large-diameter axons. This high-precision circuit in the MEC may be in place to sharpen the timing of action potentials, and to control the propagation of highly synchronous activity in a cortex that is occupied with spatial sequence analysis.

Our data are the first, to our knowledge, to demonstrate the positional sorting of output synapses in the mammalian cortex. However, in hindsight, data from the mouse visual cortex[19] and hippocampus[45] can be interpreted as an indication that PLASS may operate in various cortices. In these studies, it had been noted that the fraction of synapses targeting interneurons was higher than expected on average. Because these studies were limited in electron-microscopy-reconstructed volume (with an extent of 45 µm in the third dimension in ref. 45), the reconstructed axons were necessarily only very proximal. The fact that our volume was at least three-fold larger in the third dimension made it possible to detect PLASS as a transition from interneuron-dominated to ExN-dominated targeting within the same excitatory axons, and to determine the properties of the local cFFI circuit.

Data on axonal conduction velocity[12,46,47] and latencies of local inhibition in the cortex[43,44] make it plausible that the described circuit can prevent the propagation of highly synchronous activity in L2 of the rat MEC as shown in Fig. 6f–i (for this, propagation of action potentials along the axon would have to be between 120–240 µm ms$^{-1}$ and local inhibitory action potential-to-PSP latencies 0.5–1 ms). This is especially noteworthy because so far, feedforward inhibition circuits have been interpreted to selectively propagate synchronous, but not asynchronous activity (for example, ref. 48). By contrast, the PLASS–cFFI circuit can act as a synchrony block. At the same time, if the postsynaptic neuron was to receive additional excitatory input or an additional modulation of the underlying membrane potential, such as the theta-frequency oscillation that can be found in the MEC[49,50], the PLASS–cFFI circuit could allow a controlled, predictive gating of synchronous activity propagation (Extended Data Fig. 6d–h). The same would be possible by disinhibition of the involved interneurons.

Our data show a high-precision wiring motif in the cortex, revealing an unexpected level of structural specialization in local cortical circuits. We explored possible functional implications of these structural findings, pointing towards an effect on spike timing precision

and the control of synchronized activity propagation. Connectomic analysis of other cortices will allow us to determine if PLASS constitutes a general cortical wiring principle in mammals.

1. Kasthuri, N. et al. Saturated reconstruction of a volume of neocortex. Cell **162**, 648–661 (2015).
2. Ahmed, B., Anderson, J. C., Martin, K. A. & Nelson, J. C. Map of the synapses onto layer 4 basket cells of the primary visual cortex of the cat. J. Comp. Neurol. **380**, 230–242 (1997).
3. Holtmaat, A., Wilbrecht, L., Knott, G. W., Welker, E. & Svoboda, K. Experience-dependent and cell-type-specific spine growth in the neocortex. Nature **441**, 979–983 (2006).
4. Knott, G. W., Holtmaat, A., Wilbrecht, L., Welker, E. & Svoboda, K. Spine growth precedes synapse formation in the adult neocortex in vivo. Nat. Neurosci. **9**, 1117–1124 (2006).
5. Mishchenko, Y. et al. Ultrastructural analysis of hippocampal neuropil from the connectomics perspective. Neuron **67**, 1009–1020 (2010).
6. Koganezawa, N., Gisetstad, R., Husby, E., Doan, T. P. & Witter, M. P. Excitatory postrhinal projections to principal cells in the medial entorhinal cortex. J. Neurosci. **35**, 15860–15874 (2015).
7. van Haeften, T., Baks-te-Bulte, L., Goede, P. H., Wouterlood, F. G. & Witter, M. P. Morphological and numerical analysis of synaptic interactions between neurons in deep and superficial layers of the entorhinal cortex of the rat. Hippocampus **13**, 943–952 (2003).
8. Markram, H., Lübke, J., Frotscher, M., Roth, A. & Sakmann, B. Physiology and anatomy of synaptic connections between thick tufted pyramidal neurones in the developing rat neocortex. J. Physiol. (Lond.) **500**, 409–440 (1997).
9. Markram, H., Lübke, J., Frotscher, M. & Sakmann, B. Regulation of synaptic efficacy by coincidence of postsynaptic APs and EPSPs. Science **275**, 213–215 (1997).
10. Feldmeyer, D., Egger, V., Lubke, J. & Sakmann, B. Reliable synaptic connections between pairs of excitatory layer 4 neurones within a single 'barrel' of developing rat somatosensory cortex. J. Physiol. (Lond.) **521**, 169–190 (1999).
11. Feldmeyer, D., Lübke, J., Silver, R. A. & Sakmann, B. Synaptic connections between layer 4 spiny neurone-layer 2/3 pyramidal cell pairs in juvenile rat barrel cortex: physiology and anatomy of interlaminar signalling within a cortical column. J. Physiol. (Lond.) **538**, 803–822 (2002).
12. Helmstaedter, M., Staiger, J. F., Sakmann, B. & Feldmeyer, D. Efficient recruitment of layer 2/3 interneurons by layer 4 input in single columns of rat somatosensory cortex. J. Neurosci. **28**, 8273–8284 (2008).
13. Jiang, X. et al. Principles of connectivity among morphologically defined cell types in adult neocortex. Science **350**, aac9462 (2015).
14. Couey, J. J. et al. Recurrent inhibitory circuitry as a mechanism for grid formation. Nat. Neurosci. **16**, 318–324 (2013).
15. Fuchs, E. C. et al. Local and distant input controlling excitation in layer II of the medial entorhinal cortex. Neuron **89**, 194–208 (2016).
16. Briggman, K. L., Helmstaedter, M. & Denk, W. Wiring specificity in the direction-selectivity circuit of the retina. Nature **471**, 183–188 (2011).
17. Helmstaedter, M. et al. Connectomic reconstruction of the inner plexiform layer in the mouse retina. Nature **500**, 168–174 (2013).
18. Wanner, A. A., Genoud, C., Masudi, T., Siksou, L. & Friedrich, R. W. Dense EM-based reconstruction of the interglomerular projectome in the zebrafish olfactory bulb. Nat. Neurosci. **19**, 816–825 (2016).
19. Bock, D. D. et al. Network anatomy and in vivo physiology of visual cortical neurons. Nature **471**, 177–182 (2011).
20. Lee, W. C. et al. Anatomy and function of an excitatory network in the visual cortex. Nature **532**, 370–374 (2016).
21. Helmstaedter, M. Cellular-resolution connectomics: challenges of dense neural circuit reconstruction. Nat. Methods **10**, 501–507 (2013).
22. Denk, W. & Horstmann, H. Serial block-face scanning electron microscopy to reconstruct three-dimensional tissue nanostructure. PLoS Biol. **2**, e329 (2004).
23. Helmstaedter, M., Briggman, K. L. & Denk, W. High-accuracy neurite reconstruction for high-throughput neuroanatomy. Nat. Neurosci. **14**, 1081–1088 (2011).
24. Hua, Y., Laserstein, P. & Helmstaedter, M. Large-volume en-bloc staining for electron microscopy-based connectomics. Nat. Commun. **6**, 7923 (2015).
25. Ray, S. et al. Grid-layout and theta-modulation of layer 2 pyramidal neurons in medial entorhinal cortex. Science **343**, 891–896 (2014).
26. Kitamura, T. et al. Island cells control temporal association memory. Science **343**, 896–901 (2014).
27. Boergens, K. M. et al. webKnossos: efficient online 3D data annotation for connectomics. Nat. Methods **14**, 691–694 (2017).
28. de Vivo, L. et al. Ultrastructural evidence for synaptic scaling across the wake/sleep cycle. Science **355**, 507–510 (2017).

29. Harris, K. M. & Stevens, J. K. Dendritic spines of CA 1 pyramidal cells in the rat hippocampus: serial electron microscopy with reference to their biophysical characteristics. *J. Neurosci.* **9,** 2982–2997 (1989).
30. Arellano, J. I., Benavides-Piccione, R., Defelipe, J. & Yuste, R. Ultrastructure of dendritic spines: correlation between synaptic and spine morphologies. *Front. Neurosci.* **1,** 131–143 (2007).
31. Bopp, R., Holler-Rickauer, S., Martin, K. A. & Schuhknecht, G. F. An ultrastructural study of the thalamic input to layer 4 of primary motor and primary somatosensory cortex in the mouse. *J. Neurosci.* **37,** 2435–2448 (2017).
32. Staffler, B. *et al.* SynEM, automated synapse detection for connectomics. *eLife* **6,** e26414 (2017).
33. Beed, P. *et al.* Analysis of excitatory microcircuitry in the medial entorhinal cortex reveals cell-type-specific differences. *Neuron* **68,** 1059–1066 (2010).
34. Bruno, R. M. & Simons, D. J. Feedforward mechanisms of excitatory and inhibitory cortical receptive fields. *J. Neurosci.* **22,** 10966–10975 (2002).
35. Cruikshank, S. J., Lewis, T. J. & Connors, B. W. Synaptic basis for intense thalamocortical activation of feedforward inhibitory cells in neocortex. *Nat. Neurosci.* **10,** 462–468 (2007).
36. Kanichay, R. T. & Silver, R. A. Synaptic and cellular properties of the feedforward inhibitory circuit within the input layer of the cerebellar cortex. *J. Neurosci.* **28,** 8955–8967 (2008).
37. Eccles, J., Llinas, R. & Sasaki, K. Golgi cell inhibition in the cerebellar cortex. *Nature* **204,** 1265–1266 (1964).
38. Buzsáki, G. Feed-forward inhibition in the hippocampal formation. *Prog. Neurobiol.* **22,** 131–153 (1984).
39. Alger, B. E. & Nicoll, R. A. Feed-forward dendritic inhibition in rat hippocampal pyramidal cells studied *in vitro*. *J. Physiol. (Lond.)* **328,** 105–123 (1982).
40. Pouille, F. & Scanziani, M. Enforcement of temporal fidelity in pyramidal cells by somatic feed-forward inhibition. *Science* **293,** 1159–1163 (2001).
41. Duguid, I. *et al.* Control of cerebellar granule cell output by sensory-evoked Golgi cell inhibition. *Proc. Natl Acad. Sci. USA* **112,** 13099–13104 (2015).
42. Micheva, K. D. *et al.* A large fraction of neocortical myelin ensheathes axons of local inhibitory neurons. *eLife* **5,** e15784 (2016).
43. Hoffmann, J. H. *et al.* Synaptic conductance estimates of the connection between local inhibitor interneurons and pyramidal neurons in layer 2/3 of a cortical column. *Cereb. Cortex* **25,** 4415–4429 (2015).
44. Koelbl, C., Helmstaedter, M., Lübke, J. & Feldmeyer, D. A barrel-related interneuron in layer 4 of rat somatosensory cortex with a high intrabarrel connectivity. *Cereb. Cortex* **25,** 713–725 (2015).
45. Takács, V. T., Klausberger, T., Somogyi, P., Freund, T. F. & Gulyás, A. I. Extrinsic and local glutamatergic inputs of the rat hippocampal CA1 area differentially innervate pyramidal cells and interneurons. *Hippocampus* **22,** 1379–1391 (2012).
46. Kress, G. J., Dowling, M. J., Meeks, J. P. & Mennerick, S. High threshold, proximal initiation, and slow conduction velocity of action potentials in dentate granule neuron mossy fibers. *J. Neurophysiol.* **100,** 281–291 (2008).
47. Schmidt-Hieber, C., Jonas, P. & Bischofberger, J. Action potential initiation and propagation in hippocampal mossy fibre axons. *J. Physiol. (Lond.)* **586,** 1849–1857 (2008).
48. Bruno, R. M. Synchrony in sensation. *Curr. Opin. Neurobiol.* **21,** 701–708 (2011).
49. Alonso, A. & Klink, R. Differential electroresponsiveness of stellate and pyramidal-like cells of medial entorhinal cortex layer II. *J. Neurophysiol.* **70,** 128–143 (1993).
50. Alonso, A. & Llinás, R. R. Subthreshold Na$^+$-dependent theta-like rhythmicity in stellate cells of entorhinal cortex layer II. *Nature* **342,** 175–177 (1989).

## METHODS

**Data reporting.** No statistical methods were used to predetermine sample size. The experiments were not randomized and the investigators were not blinded to allocation during experiments and outcome assessment.

**Animal experiments.** All experimental procedures were performed according to the law of animal experimentation issued by the German Federal Government under the supervision of local ethics committees and according to the guidelines of the Max-Planck Society.

**Brain tissue preparation.** A male P25 Chbb:THOM (Wistar) rat (45 g) was anaesthetized with isoflurane. It was then perfused transcardially with ~25 ml 0.15 M cacodylate buffer, followed by ~160 ml of fixation solution (2.5% PFA, 1.25% glutaraldehyde, 2 mM CaCl in 0.08 M cacodylate buffer) at 15 ml min$^{-1}$. After perfusion, the brain was removed from the skull and left in the fixation solution for 24 h at 4 °C. Then, three consecutive parasagittal brain slices (thickness: 70 μm, 550 μm, 70 μm, respectively) containing the medial entorhinal cortex were cut from the right brain hemisphere using a vibratome (Microm HM650 V, Thermo Scientific). Next, vertical vibratome cuts were performed on the 550-μm slice to extract a ~500-μm (dorsoventral) by ~700-μm (anteroposterior) tissue sample containing the upper layers of the medial entorhinal cortex (see Extended Data Fig. 1g). This sample was further processed for en bloc electron microscopy staining.

After extraction of the electron microscopy sample, the 550-μm-thick slice was transferred into a 10% sucrose solution in phosphate buffer overnight followed by an incubation in 30% sucrose solution for 24 h for cryoprotection. After that, the brain slice was embedded in Jung Tissue Freezing Medium (Leica Microsystems Nussloch, Germany) and cut into 60-μm-thick sagittal slices with a freezing microtome (Leica 2035 Biocut). These, as well as the 70-μm-thick brain slices obtained in the previous step, were subsequently processed for calbindin immunoreactivity to confirm the sample location within the MEC (Extended Data Fig. 1g).

To obtain the P90 sample, the same procedure was applied. In brief, a 90-day-old Wistar rat (235 g) was anaesthetized with isoflurane, then perfused transcardially with ~75 ml 0.15 M cacodylate buffer, followed by ~250 ml of fixation solution at 15 ml min$^{-1}$. The ~600 × 700 μm sample was extracted from a 500-μm-thick parasaggital brain slice containing the upper layers of the MEC and processed for electron microscopy (see below). After sample extraction, the slice was processed for calbindin immunoreactivity to confirm the sample location within the MEC (Extended Data Fig. 1h).

**Calbindin immunohistochemistry.** The staining for calbindin was performed as described previously[25]. In brief, brain sections were incubated with (in the following sequence): blocking solution (0.1 M PBS, 2% bovine serum albumin (BSA), 0.5% Triton X-100 (PBS-X) for 1 h at room temperature); primary antibodies (24 h at 4 °C; anti-calbindin (Swant; 1:50,000 in PBS-X and 1% BSA)); secondary antibodies coupled to Alexa 488 (Invitrogen) (1:500 in PBS-X for 2 h in the dark at room temperature). After staining, sections were mounted on gelatin-coated glass slides with Vectashield mounting medium (Vectorlabs: H-1000).

**Sample preparation for electron microscopy.** En bloc staining for electron microscopy was performed as in ref. 24. In brief, the tissue was stained with a reduced osmium tetroxide solution (2% OsO$_4$ in 0.15 M cacodylate buffer) followed by incubation with ferrocyanide (2.5% KFeCN in 0.15 M cacodylate buffer) and an incubation in saturated aqueous thiocarbohydrazide solution. The sample was then transferred into 2% OsO$_4$ (in H$_2$O) for amplification and was subsequently left overnight at 4 °C in a solution containing 2% uranyl acetate (in H$_2$O). Then, the tissue was incubated in 0.02 M lead(II) nitrate. Dehydration and resin embedding was performed as in ref. 16. In brief, the sample was dehydrated with propylene oxide and ethanol, infiltrated with 50%/50% propylene oxide/Epon and embedded in Epon (using the Epon substitute embedding medium kit, Sigma-Aldrich) at 60 °C for 24 h. For the P90 sample, embedding was as described in ref. 24.

**Continuous imaging.** The P25 sample was imaged using a Magellan scanning electron microscope (FEI Company) equipped with a custom-built SBEM microtome (courtesy of W. Denk). To allow continuous image acquisition, piezo actors (P-602 Physik Instrumente) were added to the microtome setup to operate in line with geared motors (M-230, Physik Instrumente; Extended Data Fig. 1b) for movements in the plane of imaging ($x$ and $y$ directions).

The plane of imaging was divided into four overlapping regions (motortiles; Extended Data Fig. 1c) with a size of 217 μm for the $x$ axis and 216 μm for the $y$ axis, each (note that the radial cortex axis corresponded to the horizontal ($x$) axis during image acquisition). The stage movement between the motortiles was executed using the geared motors. Within each motortile, stage movement was executed using the piezo actors and configured as follows (Extended Data Fig. 1d–f). The vertical stage movement ($y$ axis) consisted of a brief acceleration to 34.2 μm s$^{-1}$ followed by a plateau continuous movement for 7.5 s, followed by a linear deceleration to −34.2 μm s$^{-1}$ (see the piezo-control voltage transients

during one motortile). This corresponded to continuous alternating down- and upwards movements (piezo columns), interleaved by direction inversions. The horizontal stage movement ($x$ axis) was executed during the direction-inversion strokes, yielding stepwise rightward movements in the $x$ direction after each piezo column that shifted the piezo columns by 31.4 μm. After each piezo column, the image orientation was rotated by 90° using the image rotate option in the FEI control software.

After acquisition of the first motortile, the stage was moved rightwards by 217 μm, and then the 2nd motortile was executed, this time starting from the bottom right of the motortile area such that the positions of the piezo actor do not have to be changed between the end of motortile 1 and the beginning of motortile 2. Then, motortiles 3 and 4 were executed analogously.

Image acquisition was configured as follows: during the piezo-column movements, 10 images with a size of 2,048 × 3,072 voxels each were acquired continuously (without delay between image acquisitions) using a custom-written C# library (KMB, B. Lich and P. Potocek). Image acquisition was started 0.59 s after initiation of the piezo-column movement. To compensate for the line feed introduced by the $y$ piezo movement, the electron microscopy scanning line feed was reduced to 7.1% by activation of the 'tilt' mode (set to 85.9°). The reset movement of the electron microscopy beam after image acquisition therefore amounted to a beam position jump antiparallel to the current $y$ piezo movement, creating overlap between consecutive images in the $y$ axis that could later be used for image alignment (see below). After image acquisition during one piezo-column movement, image acquisition was paused for 1.08 s to allow the movement of $x$ axis piezo to be executed. The resulting image columns had a variable offset along the $y$ axis (Extended Data Fig. 1c) that was compensated for by an overlap between the motortiles of about 8 μm, such that complete coverage of the blockface was assured.

Seven consecutive piezo columns were spaced in the $x$ direction such that neighbouring columns overlapped by about 9% in the horizontal direction. Motortiles were set to overlap by about 5.5 μm in $x$ axis direction. Dwell time was set to 100 ns, and the effective data-acquisition speed, including all overheads, was 5.9 MVx s$^{-1}$.

**Conventional mosaic imaging.** The P90 sample was imaged using a Quanta scanning electron microscope (FEI, Quanta 250 FEG) equipped with a custom built SBEM microtome (courtesy of W. Denk). Image acquisition was performed in the conventional mosaic-based mode. The plane of imaging was divided into 4 × 2 overlapping regions, each with a size of 46 × 69 μm. The stage movement between these mosaics was performed using geared motors (M-227.25, Physik Instrumente). Overlap between mosaic positions was set to 1.1–2 μm. Dwell time was set to 2.3 μs, and the effective data-acquisition speed, including movement overheads, was 0.4 MVx s$^{-1}$.

**Dataset acquisition.** For the P25 dataset, the sample position was centred to L2 judged by the distance to the pia in low-resolution overview images, and acquisition in continuous mode (see above) was started. Subsequently, 8,372 consecutive image planes were acquired, interleaved by microtome cuts set to a cutting thickness of 30 nm. For the final 56 μm of the dataset, cutting thickness was set to 50 nm, therefore the total thickness of the dataset in the cutting direction was approximately 274 μm (see 'Image alignment'). The incident electron energy was set to 2.5 keV for the first 561 slices, then increased to 2.8 keV. The beam current settings were chosen to yield 3.2 nA nominal beam current (resulting in a dose of approximately 16 electrons nm$^{-2}$). Focus and astigmatism were constantly monitored and adjusted for using custom-written autofocus routines. Focus was frequently unstable, probably owing to cutting debris accumulating around the sample and in the vacuum chamber. This was compensated for by frequent manual skeleton reconstruction with about 3-h intervals during the course of the experiment to monitor axon traceability. The position of the field of view was shifted four times during the course of the experiment to compensate for a tilt of the sample in the tangential plane (shifts along the radial cortex axis towards white matter by 17.5 μm from plane 1,816 onwards, by 21.6 μm from plane 3,146, by 43.1 μm from plane 4,336 and by 24.8 μm from plane 6,375).

The field of view of the P90 sample was centred to L2 of the MEC, containing parts of L3. In low-resolution overview images, the beginning of L2 is clearly distinct from the almost cell-free L1. Subsequently, 5,545 consecutive image planes were acquired, interleaved by microtome cuts set to a cutting thickness of 30 nm. For the final 262 slices of the dataset, the field of view was shifted by ~112 μm towards the pia to compensate for a slight tilt of the sample in the tangential plane. The incident electron energy was set to 2.8 keV. The beam current settings were chosen to yield a nominal beam current of 0.16 nA (resulting in a nominal dose of approximately 22.27 electrons nm$^{-2}$). Focus and astigmatism were constantly monitored and adjusted 2–4 times per day.

**Image alignment.** All images obtained from one image plane and motortile (that is, 10 × 7 = 70 images with a size of 2,048 × 3,072 voxels each) were aligned separately using Speeded Up Robust Features (SURF) that were detected on the

overlap regions of neighbouring image pairs (P25). For the P90 dataset, in plane alignment was performed with FIJI/ImageJ using the 'grid/collection stitching' plugin[51].

To match aligned images from consecutive planes, a region with a size of 70% of the horizontal motortile size and 50% of the vertical motortile size, located at the motortile centre, was cross-correlated with the same region from the next image plane. The translation vector between the cross-correlation peaks was applied to the second image, respectively. For 565 slices (P25), debris from previous cuts was present on the block surface. These slices were excluded from alignment, yielding a total of 7,807 slices that were used for reconstruction. For the P90 dataset, the first 3,399 slices were used for reconstruction (24 slices were excluded because of debris, yielding a total of 3,375 slices).

After alignment, the four resulting three-dimensional image stacks for each of the four motortiles (subsequently referred to as MT1 to MT4) of the P25 dataset, as well as the aligned image stack of the P90 dataset, were each converted to the KNOSSOS data format[23,27] (see https://webknossos.org) by splitting the data into data cubes with a size of $128 \times 128 \times 128$ voxels each. These data were then uploaded to our online data annotation software webKnossos[27] for in-browser distributed data visualization, neurite skeletonization and synapse identification.

**Myelin reconstruction.** For the analysis of the myelination pattern in the tangential plane (Extended Data Fig. 3b) in order to identify myelin-free patches, all myelinated axons were skeleton reconstructed in webKnossos by student annotators. First, seed points were placed in cross sections of myelinated axons in plane 17 of MT2 and MT4, and myelinated axons reconstructed from these seed points. After completion, additional seed points were placed into unreconstructed myelinated axons that were found in plane 6,000 of MT2 and MT4. This was repeated for cutting plane 3,000 in the middle part of the dataset. When reconstructing myelinated fibres, annotators were instructed to also mark intermediate unmyelinated segments. All skeleton tracings that were between 110 and 200 μm from the pia were then projected into the tangential plane (Extended Data Fig. 3b), excluding those skeleton segments marked as unmyelinated. The synapse distance to patch centres was evaluated in the tangential plane (Extended Data Fig. 3c, d).

**Reconstruction of axons and dendrites.** We identified 665 neuronal cell bodies in all four motortiles of the P25 dataset and reconstructed all dendrites with the help of 24 undergraduate students using webKnossos[27]. Annotators were instructed to reconstruct all dendrites starting from the soma without spines, to be especially cautious as not to miss branches and to place comments whenever the dendrite reached a motortile border for subsequent matching of neurites across motortiles. All students were trained on at least three neurons, including 1–2 cells from this MEC dataset (total training time about 10 h per student). Only after successfully finishing training the annotators were allowed to continue with new tasks. The same procedure applied to the reconstruction of the 91 identified neuronal cells in the P90 dataset.

All axons in the P25 dataset were reconstructed by one expert annotator; one axon was independently reconstructed by two additional expert annotators, whose results agreed with the original annotation. Axons were terminated either at the border of the dataset, by an axonal termination (which was always found in an end-bouton synapse) or because they could not be followed further owing to focus issues.

All axons in the P90 dataset were reconstructed independently by two expert annotators and 10 undergraduate students. The two expert tracers then formed a consensus reconstruction based on the 12 annotations per axon.

To match dendrites and axons across motortiles of the P25 dataset the following procedure was applied. The dendrite or axon was identified in the overlap region of the adjacent motortile. Prominent processes, such as myelinated fibres, somata and large-diameter dendrites in the same cutting plane, were used as landmarks to constrain the search region. The first node of the continuing process was then placed at the same position within the neurite. The difference between the coordinates of these two matching points was then used to transform the skeletons into one coordinate system for further analysis. This procedure was repeated whenever the tracing reached a motortile border. All axons and all dendrites of the 15 excitatory neurons and 3 inhibitory cells (shown in Figs 2, 5) were reconstructed completely across all motortiles.

**Synapse identification and target classification.** Synapses were identified by following the trajectory of axons in webKnossos[27]. First, vesicle clouds in the axon were identified as accumulations of more than about 10 vesicles. Subsequently, the most likely postsynaptic target was identified by the following criteria: direct apposition with vesicle cloud; presence of a darkening and broadening of the synaptic membrane, indicative of a postsynaptic density; vesicles very close to the membrane at the site of contact (see Fig. 1 for examples and ref. 32). Synapses were classified as uncertain whenever the signs of a broadened and darkened stain at the synaptic membrane (resembling a postsynaptic density) could not be clearly identified. All analyses in this study were conducted only on synapses that had been classified as certain. To measure inter-expert variability in synapse annotation, three additional experts annotated all synapses and their targets for one of the ExN axons (Fig. 2b, 7th row). For each of the four expert annotations, independently, PLASS was found (the path-length-distribution of synapses onto spines and synapses onto shafts was significantly different, $P < 0.02$, 0.01, 0.04, 0.03, respectively). Out of 44 synapses, 39 were identified as certain by all four annotators, three additional synapses by 3 out of 4 annotators, and two by 2 out of 4 annotators. For the P90 dataset, two additional experts independently annotated 30 randomly selected synapses (agreement with the initial expert annotator: 28 out of 30 and 30 out of 30 for the two experts, respectively).

The postsynaptic targets of axonal synapses ($n = 310$, P25; $n = 284$, P90) were classified as ExN, interneuron or glia (for each apparent postsynaptic spine head, the corresponding dendritic trunk was searched to distinguish from glial targets). For this, the target dendrites were identified by the corresponding soma, which had been reconstructed before and classified as ExN or interneuron. For the classification as ExN or interneuron, dendrite morphology and the origin of the axon was evaluated. ExN axons exited the soma towards the white matter, whereas interneuron axons frequently originated from dendrites. For the remaining targets, the postsynaptic dendrites were classified as smooth or spiny by reconstructing them at least in one motortile/whole volume (P90) and measuring the rate of spines on two 10-μm-long dendritic segments. Dendrites were either clearly spiny, carrying few spines and filopodial protrusions without a clear spine head or lacking spines entirely. We used dendrites of clearly identified interneurons and ExNs to calibrate spine density, yielding a definition of spiny dendrites with a spine density of $\geq 0.6$ per μm, and smooth dendrites with a spine density of $\leq 0.2$ per μm.

**Calibration of synapse size.** To calibrate the distribution of synapse size obtained in our data in comparison to published data, we randomly selected 20 synapses made onto spines in the P90 dataset. We then manually volume labelled the spine heads in webKnossos[27], imported the voxel map into MATLAB, scaled the data by voxel size, applied 3D smoothing and measured the contained volume. Similarly, the axon–spine interface for these synapses was annotated by drawing lines along the interface in each successive image plane (as in ref. 28). The axon–spine interface area was then calculated as the path length of the annotated lines multiplied by the cutting thickness.

**Dense dendritic reconstruction and dendrite density measurement.** For the measurement of interneuron dendrite density in the P25 dataset, seven regions with a size of $10 \times 10 \times 10\,\mu m^3$ each were selected along the radial cortex axis within L2 (Extended Data Fig. 3e, f). Regions were chosen to avoid cell bodies or blood vessels. Within these regions, all dendritic shafts were densely skeleton reconstructed. Then, each dendrite was classified as smooth or spiny based on the above criteria. When a dendrite did not show spines locally, it was followed for at least 10 μm. If none or 1–2 spines were found, the dendrite was continued for at least 30–40 μm to ensure that there were no spiny regions. Only then the dendrite was classified as smooth/interneuron. Dendrite path length was measured from the reconstructed shaft skeletons (thus excluding spine path length).

**Pyramidal and stellate cell classification.** Two previously reported[15] parameters for classification of pyramidal versus stellate cells in MEC L2 were investigated: the number of primary dendrites and the size of the cell body. Two experts were asked to assign the morphology of dendritic reconstructions as clear pyramidal, clear stellate or unsure. For 29 out of 67 reconstructions, both experts agreed in the assignment to the high-confidence categories (Extended Data Fig. 2). For these neurons, the soma volume (Fig. 1i, j) was measured by placing two nodes in each of the three orthogonal viewports in webKnossos[27] to mark the extent of the three main axes, of which the geometric mean was used for volume approximation. In addition, the number of primary dendrites was counted for a subset of 15 neurons (six clear pyramidal cells, four clear stellates, five intermediate cells; Fig. 2b), but this was not found to be distinctive. The distributions of soma size (Fig. 1i) were each fitted by a Gaussian, and the probability of a neuron belonging to the clear stellate cell class, $P_{stellate}$, was calculated by dividing the Gaussian fit to the soma diameters of stellate cells by the sum of both fits.

**Local circuit analysis.** Local circuit analysis was based on the connectivity data reporting the number of synapses between pairs of neurons or neurites (Supplementary Information 1) in the P25 dataset. The synaptic connectivity between the four largest ExN axons, three fully reconstructed interneurons and 58 ExN targets that had their soma in the dataset was analysed. In brief, the connectivity matrix between these neurons was binarized to represent the presence or absence of synaptic connectivity. Then, indirect triadic connections of ExN–interneuron–ExN were identified by squaring the connectivity matrix with all ExN–ExN connections set to zero. Then all full cFFI triads were identified by element-wise multiplication of the squared connectivity matrix with the ExN–ExN connectivity matrix. The resulting number of cFFI configurations ($n = 31$) was then divided by the total number of ExN–ExN connections ($n = 41$), yielding a 76% cFFI ratio. A MATLAB script used for this analysis based on the data in Supplementary Information 1 is provided in Supplementary Information 2.

**Axon diameter measurements.** Contours of axonal cross sections (Fig. 5g) were reconstructed from all axonal branches at a distance of 170 μm from the soma of six ExN axons (four from P25, two from P90) and four interneuron axons (three from P25, one from P90, 74 contours in total) using webKnossos[27]. Contours were traced in the orthogonal viewport most perpendicular to the local axon axis.

The diameter of axons was measured for the four excitatory axons with the highest path length and three interneuron axons in the P25 dataset; and for three excitatory neurons and one interneuron axon in the P90 dataset. To obtain the analyses shown in Fig. 5h, for the ExN axons, four synapses onto ExN targets were chosen, each (16 synapses in P25, 12 synapses in P90); of the four synapses chosen per axon, three were randomly drawn, and one was at a close-to-maximum path length distance from the soma. Then, for each synapse, skeleton nodes that were 25 μm apart were selected along the path from that neuron's soma to the respective synapse and the diameter of the axon was measured at these locations in webKnossos[27]. In case of myelinated segments, the inner unmyelinated axon diameter was measured. In case of branch points the diameter was measured slightly before the branch point. This procedure was similar for the six synapses from each of the three inhibitory axons in P25 and the seven synapses from one inhibitory axon in P90. All measurements are shown in Fig. 5h (P25) and Extended Data Fig. 5b (P90). For reporting mean and s.e.m., diameter measurements were linearly interpolated, and mean and s.e.m. were calculated for 0 to 400 μm distance from the cell body at 25-μm intervals (Fig. 5h). For comparison of axon diameters between excitatory and inhibitory axons, the average diameters were computed between the point where the interneuron axons started their main branches, and the point where most synapses were made (defined as the range between the position of the 4th axonal branch point and the point at which 10% of the cumulative output synapses (from all interneurons) were reached; these ranges were 134–261 μm, P25; and 83–188 μm, P90).

**Estimates of local circuit convergence and divergence.** Bounds on local circuit convergence and divergence (used for circuit modelling, Fig. 6 and Extended Data Figs 4, 6) were estimated as follows: for divergence of excitatory projections onto local interneurons, we used as a lower bound the number of unique interneurons (with identified soma in the dataset) that were targeted by the largest six presynaptic axons in P25 (each more than 600 μm in length); this was five per axon. We then asked how many synapses were likely to have been made between a given connected pair of excitatory and inhibitory neurons. This number was 2.6 in P25 for identified ExN-to-interneuron connections; but about 4 at P90 (assuming that single-hit connections were due to artificially pruned axons, because no such connections are reported in the literature). We then scaled the total number of synapses made onto interneurons per ExN axon to an expected local ExN axon path length of about 2 mm (based on the probable local truncations and inspection of single-cell fills in ref. 52), and divided this by the number of synapses per connection (about 40–50 synapses onto interneurons divided by 4 yields a divergence of about 10–12 interneurons). We then screened the circuit models using an ExN-to-interneuron divergence of 5–10 interneurons. We did not use higher interneuron numbers, because at the same time the effective conductance in the interneuron-to-ExN connection was screened between 950 and 1,950 pS per contact (see below), yielding an additional range of factor 2. For the estimate of ExN-to-ExN convergence, we did not use our measured synapse numbers, because we had found that ExN outputs are positioned more distally in the presynaptic axons (Fig. 2), making it likely that most ExN-to-ExN connectivity is established beyond our local reconstructions. Instead, we used the reported connectivity from ref. 15, which ranged from about 5 to 10% local ExN-to-ExN connectivity. Given about 600 local ExNs (about 90% of about 660; Fig. 1), this yields 30–60 ExN that converge onto a postsynaptic ExN. We used 60 and 40 in the two main simulations (Fig. 6 and Extended Data Fig. 4), and screened stability over ExN populations from 20–80 (Extended Data Fig. 4h, i).

**Numerical simulations.** Numerical simulations were performed using NEURON v.6.2 on a compute cluster (CentOS Linux 7). Morphologies of seven interneurons and four pyramidal cells from rat cortical layer 2 were converted to piecewise cylindrical approximation and loaded into NEURON as described previously[53].

Passive and active electrical parameters were fitted to the measured electrical properties to reproduce the axonal initiation, timing, threshold and shape of action potentials *in vitro*. In brief, the passive membrane properties were first fitted by adjusting the membrane leak conductance, the reversal potential of the membrane leak current and the membrane capacity in an iterative procedure. For the L2 pyramidal-cell models the average (mean ± s.d.) experimental and simulated values of the input resistance, the resting membrane potential and the membrane time constant were 72.12 ± 8.74 MΩ (simulated: 74.76 ± 11.22 MΩ), −76.27 ± 2.70 mV (simulated: −76.92 ± 2.65 mV) and 14.90 ± 2.69 ms (simulated: 16.36 ± 4.53 ms), respectively. For the L2/3 interneuron models the corresponding values were 66.29 ± 22.06 MΩ (65.95 ± 28.88 MΩ), −71.68 ± 4.48 mV (−72.97 ± 3.53 mV) and

5.85 ± 1.68 ms (4.95 ± 1.60 ms). Subsequently, the active membrane mechanisms were adjusted such that the simulated somatic voltage responses to two 200-ms long step current injections (a threshold and a suprathreshold stimulus) would fit the corresponding voltage traces recorded *in vitro*. The respective amplitudes were 0.26 ± 0.05 and 0.31 ± 0.05 nA for the pyramidal-cell models and 0.38 ± 0.11 and 0.57 ± 0.12 nA for the interneuron models. For each model a total of 24 parameters were optimized in parallel defining the active conductances that were used.

For the investigation of population versus cellular feedforward inhibition (pFFI versus cFFI; Extended Data Fig. 4), the following simulations were performed. First, the time points of the occurrences of action potentials in a pool of 60 presynaptic excitatory neurons within a 30-ms interval were drawn from a Poisson distribution with a probability of 0.08 action potentials per cell per ms. Two such pool activations were drawn, one as input to the interneuron pool, one as input to the postsynaptic excitatory neuron ($ExN_{post}$) pool when simulating pFFI. To emulate cFFI, the pool activation used for input to the interneuron pool was identically used as input for $ExN_{post}$. Second, all neurons in the presynaptic pool ($ExN_{pre}$) were synaptically coupled to each of the seven neurons in the interneuron pool using NetCon triggered at the time points of the presynaptic action potentials. The NetCon were connected to an Exp2Syn synapse model with parameters 0.36 ms, 1.1 ms, and 0 mV for $\tau_1$, $\tau_2$ and $E_{syn}$, respectively. The peak synaptic conductances were set to 350 pS per synapse. The number of synapses per connected $ExN_{pre}$-to-interneuron cell pair was drawn from a normal distribution centred at 4 with a standard deviation of 1. All synapses were modelled to converge on the soma for simplicity.

We then simulated the integration of these presynaptic inputs in the postsynaptic interneuron models and detected the time points of action potentials in the interneuron at the maximum voltage in the interval between two consecutive crossings of a membrane potential of 0 mV.

Third, we simulated the convergence of the synaptic inputs from the $ExN_{pre}$ pool and interneuron pool onto $ExN_{post}$. For this, the input from the neurons in the interneuron pool was simulated by connecting two Exp2Syn per contact to emulate double-exponential GABAergic synaptic kinetics[43], using the GABAergic synaptic parameters as in ref. 43. The total synaptic conductance per synapse was varied between 950 pS and 1,950 pS to represent the accumulated variability of the inhibitory branch of the cFFI circuit: ExN-to-interneuron divergence was taken as 5–10 (see above), which is probably a lower bound, and could in fact be 10–20; the number of contacts in the interneuron-to-ExN connection was found to be 3.5 in our data (see below), which is a strict lower bound; other data from interneuron-to-ExN connections in the cortex indicates a range of 5–15 contacts per connection[43,54,55]. The synaptic delay in the inhibitory axon (interneuron-to-$ExN_{post}$) was set to 1 ms. The number of synapses per connected interneuron-to-$ExN_{post}$ cell pair was drawn from the measured distribution of contact numbers (3.54 ± 1.8). The input from the neurons in the $ExN_{pre}$ pool was simulated by one Exp2Syn synapse model per contact with the same parameters as for the connection onto interneurons, except for the peak synaptic conductance, which was set to 720 pS. The number of synapses per connected $ExN_{pre}$-to-$ExN_{post}$ cell pair was drawn from the measured distribution of contact numbers (2.33 ± 0.67). Then, the membrane potential in the $ExN_{post}$ neurons was simulated, and the time points of action potentials recorded and evaluated. These simulations were sampled in 2,000 runs of input to each of the seven interneurons, each time sampling a new presynaptic activity set.

For the investigation of the relative effects of PLASS-related and inhibition-related delays (Fig. 6f–i), we made the following adaptations to the models described above. First, the presynaptic excitatory pool size was reduced to 40 cells (emulating that 2 out of 3 of a given set of presynaptic neurons undergo the synchronous activity described here). Second, we generated distributions of action potentials in this cell pool by uniformly randomly distributing one action potential per cell within an interval $\Delta t_{sync}$ of 3 and 10 ms. A total of five different interneuron models were used to simulate the interneuron pool. The number of synapses per connected $ExN_{pre}$-to- interneuron cell pair was drawn from the measured distribution of contact numbers (4 ± 3.1, range 2–16). The peak synaptic conductance per inhibitory interneuron-to-$ExN_{post}$ synapse was 950 pS. Then, the following additional delays were implemented: for the transmission of interneuron-to-$ExN_{post}$, an explicit delay of $\Delta t_{inh}$ was added between the time point of the action potential in the interneuron and the beginning of the IPSP in $ExN_{post}$. Similarly, the beginning of the excitatory PSP in the $ExN_{post}$ was delayed compared to the onset of the excitatory PSP in the interneurons by an additional interval $\Delta t_{PLASS}$ as indicated in Fig. 6. The simulation of $ExN_{post}$ also involved recording the subthreshold voltage response for Fig. 6h. A total of 20,200 simulation runs were made, sampling five interneuron models, four pyramidal-cell models, 100 distributions of presynaptic action potentials, $\Delta t_{inh}$ = 0.5, 0.7, 1, 1.5, 2, 30 ms, $\Delta t_{PLASS}$ = 1, 0.5, 0.25, 0 ms and $\Delta t_{sync}$ = 3, 10 ms.

**Statistical tests.** All statistical tests were performed using MATLAB and the Statistics Toolbox Release 2014b, 2015b or 2016a (The MathWorks, Inc.). The distributions of soma volume for pyramidal versus stellate cells (Fig. 1i) were compared using a two-sided $t$-test for unpaired samples (function ttest2) and, because of small sample sizes ($n = 15, 14$), using a Wilcoxon rank-sum test (function ranksum). The distributions of output synapse locations for inhibitory versus excitatory targets (Fig. 2c, f and Extended Data Fig. 3a) were compared using a two-sided $t$-test for unpaired samples ($n = 136$ and $140$, Fig. 2c; $n = 90$ and $189$, Fig. 2f); a Wilcoxon rank-sum test (function ranksum) as well as a randomization test for 1,000 random draws (random shufflings of the target assignment for all measured synapse positions; none of the 1,000 draws yielded a class separation equal to or larger than the observed separation between synapses onto interneuron and ExN targets, Fig. 2c, f). Gaussian curves were fit to the initial peak of each distribution by constraining the fit range to 0–300 μm (output to interneurons) and 0–400 μm (output to ExNs) in Fig. 2c, and to 0–250 μm (output to interneurons) and 0–400 μm (output to ExNs) in Fig. 2f. The test of the Euclidean distances of the excitatory versus inhibitory synapses to the soma (Fig. 2g) was performed as a two-sided $t$-test for unpaired samples ($n = 136$ and $140$) as well as a Wilcoxon rank-sum test. Interneuron dendrite fraction over cortical depth (Extended Data Fig. 3e, f) was fitted by a line fit ($n = 7$ datapoints, fit in MATLAB) yielding a linear approximation of the slope $-0.08/100$ μm and $y$-axis intersection at 0.36.

For the statistical comparison of cFFI versus opponent inhibition (Fig. 3a–c), the following model was used. Given a triad of connections ExN$_i$-to-ExN$_j$ and ExN$_i$-to-interneuron (of which we had 114 in our data), only two cases can follow: either the connection interneuron-to-ExN$_j$ also exists (corresponding to cFFI, 54 cases in our data), or not (corresponding to opponent inhibition, 60 cases in our data). Assume an underlying biological probability $P_b$ that interneuron-to-ExN$_j$ exists ($P_b = 0$ would correspond to strict opponent inhibition; $P_b = 1$ to strict cFFI; $P_b = 0.25$ could be interpreted as opponent inhibition with a biological wiring noise of 25%, a level of wiring noise seen in, for example, ref. 17). Furthermore, the truncation of interneuron axons yields a connection detection probability $P_{det}$ (this we estimated to be about 70% based on the completeness of the axonal trees of the interneurons; Extended Data Fig. 5a). Together, the model implies a probability $P_{meas} = P_b \times P_{det}$ of finding the connection interneuron-to-ExN$_j$ in a given triad. Then, $10^7$ sets of 114 triads were drawn, and the cases recorded in which at least 54 out of 114 triads had the additional ExN$_j$-to-interneuron connection, in dependence of $P_b$ and with $P_{det} = 65\%$, 70%, 75%. A strict opponent inhibition model ($P_b \approx 0$) was refuted at $P < 10^{-7}$, as were connection probabilities of $P_b$ up to 30% (interpretable as opponent inhibition with 30% wiring noise).

But even the chance model $P_b = 0.5$ was refuted at $P = 7 \times 10^{-4}$, $P = 4 \times 10^{-3}$, $P = 0.02$ for $P_{det} = 65\%$, 70%, 75%, respectively, due to the limited detection probabilities $P_{det}$.

The effect of cFFI versus pFFI on the width of the timing distribution of postsynaptic action potentials and the number of action potentials (Extended Data Fig. 4e–g) was compared using a two-sided $t$-test for unpaired samples (function ttest2). There, the mean and s.d. was calculated by dividing the total of 8,000 simulations (2,000 trials per cell) into $n = 20$ blocks of 400 trials each (100 trials per cell).

The comparison of path-length positions of interneuron output synapses involved in cFFI circuits with all output synapses of interneurons (Fig. 5c) was performed using a two-sided $t$-test for unpaired samples ($n = 884$ and $131$). The distribution of excitatory versus inhibitory axon diameters (Fig. 5h, inset and Extended Data Fig. 5b) were compared using a two-sided $t$-test for unpaired samples ($n = 15$ and $18$) and Wilcoxon rank-sum test. The test of the bias in number of inhibitory synapses over excitatory synapses in the convergent cFFI circuits (Fig. 6c) was performed as a one-sided, right-tailed, $t$-test (function ttest) of the relative interneuron/ExN number of synapses per connection against 1 ($n = 54$ circuits). The distribution of dendritic Euclidean distance of excitatory versus inhibitory synapses onto the converging cell (Fig. 6d), as well as the path-length distribution of inhibitory versus excitatory synapses of the same presynaptic axon (Fig. 6e), were compared over all $n = 54$ cFFI circuits using a two-sided $t$-test for paired samples (function ttest2).

**Code availability.** Code for the analysis of the cFFI circuit data (Supplementary Information 1) is available in Supplementary Information 2. All code used for the numerical simulations (Fig. 6 and Extended Data Figs 4, 6) is available at http://plass.brain.mpg.de.

**Data availability.** All image data and reconstructions are available at http://plass.brain.mpg.de.

51. Preibisch, S., Saalfeld, S. & Tomancak, P. Globally optimal stitching of tiled 3D microscopic image acquisitions. *Bioinformatics* **25,** 1463–1465 (2009).
52. Burgalossi, A. *et al.* Microcircuits of functionally identified neurons in the rat medial entorhinal cortex. *Neuron* **70,** 773–786 (2011).
53. Helmstaedter, M., Sakmann, B. & Feldmeyer, D. The relation between dendritic geometry, electrical excitability, and axonal projections of L2/3 interneurons in rat barrel cortex. *Cereb. Cortex* **19,** 938–950 (2009).
54. Gupta, A., Wang, Y. & Markram, H. Organizing principles for a diversity of GABAergic interneurons and synapses in the neocortex. *Science* **287,** 273–278 (2000).
55. Markram, H. *et al.* Interneurons of the neocortical inhibitory system. *Nat. Rev. Neurosci.* **5,** 793–807 (2004).

**a** P90

**b**

**c**

**d**

**e**

**f**

**g**

**h**
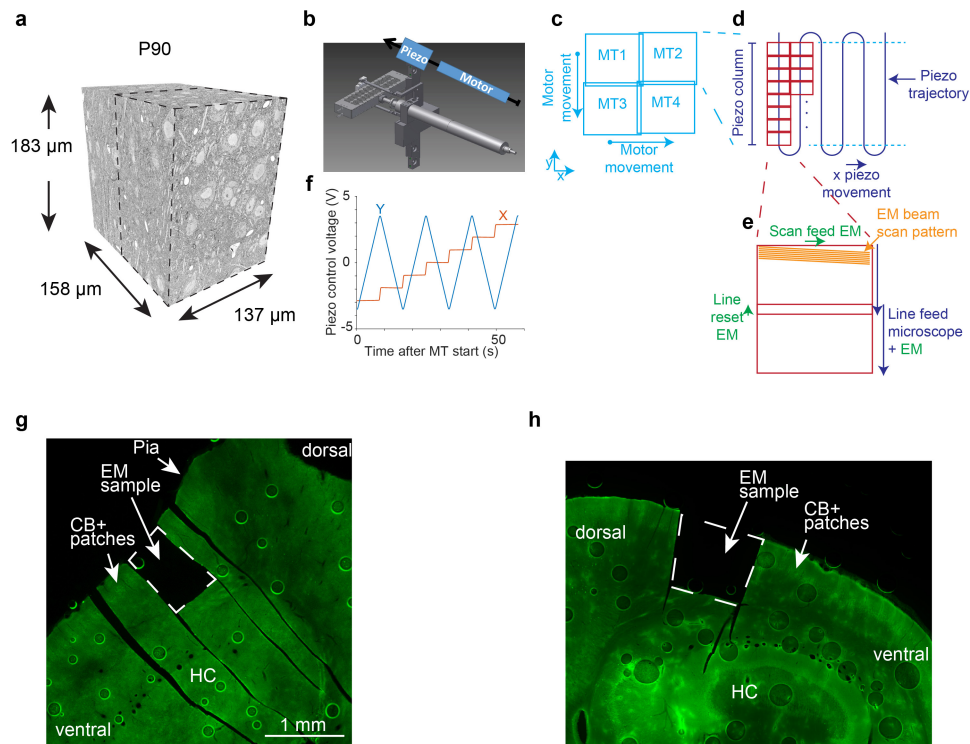
**Extended Data Figure 1 | P90 dataset, continuous SBEM imaging and calbindin (CB) immunohistochemistry. a**, Dimensions of the P90 SBEM dataset (pia, top). Dashed bounding box: initial 101 μm in $z$ after which the analysis was started. **b–f**, Continuous SBEM imaging. **b**, Sketch of microtome with piezo actor installed in-line with the geared motor (see Methods). **c–e**, Sketch of the stage movement and imaging setup in continuous SBEM imaging. **f**, Piezo actor command voltages during one motortile acquisition. See Methods for details. **g**, **h**, Confirmation of sample location in the dorsal MEC. Post hoc CB$^+$ staining of the remaining tissue after electron microscopy (EM) sample extraction for the P25 dataset (**g**) and P90 dataset (**h**). CB$^+$ patches are visible close to the pia. HC, hippocampus.
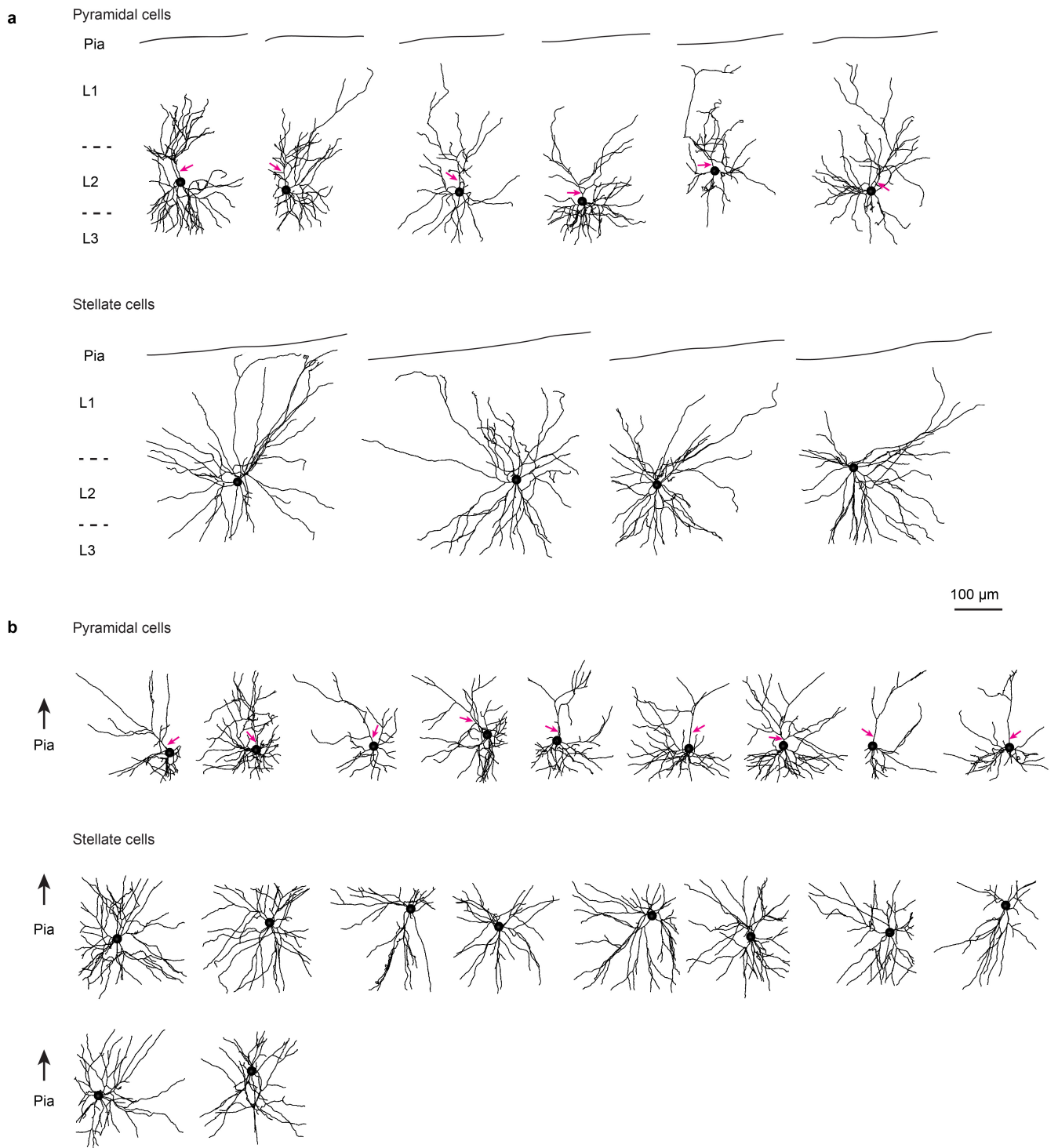
**Extended Data Figure 2 | Gallery of electron-microscopy-based reconstructions from P25 dataset. a**, Pyramidal cells (top) and stellate cells (bottom) for which expert consensus was reached about cell-type classification. Note apical dendrites (magenta arrows) and denser plexus of basal dendrites for pyramidal cells, and lack of a clear apical dendrite for stellate cells. **b**, Same for locally reconstructed neurons. Scale bar, 100 μm.
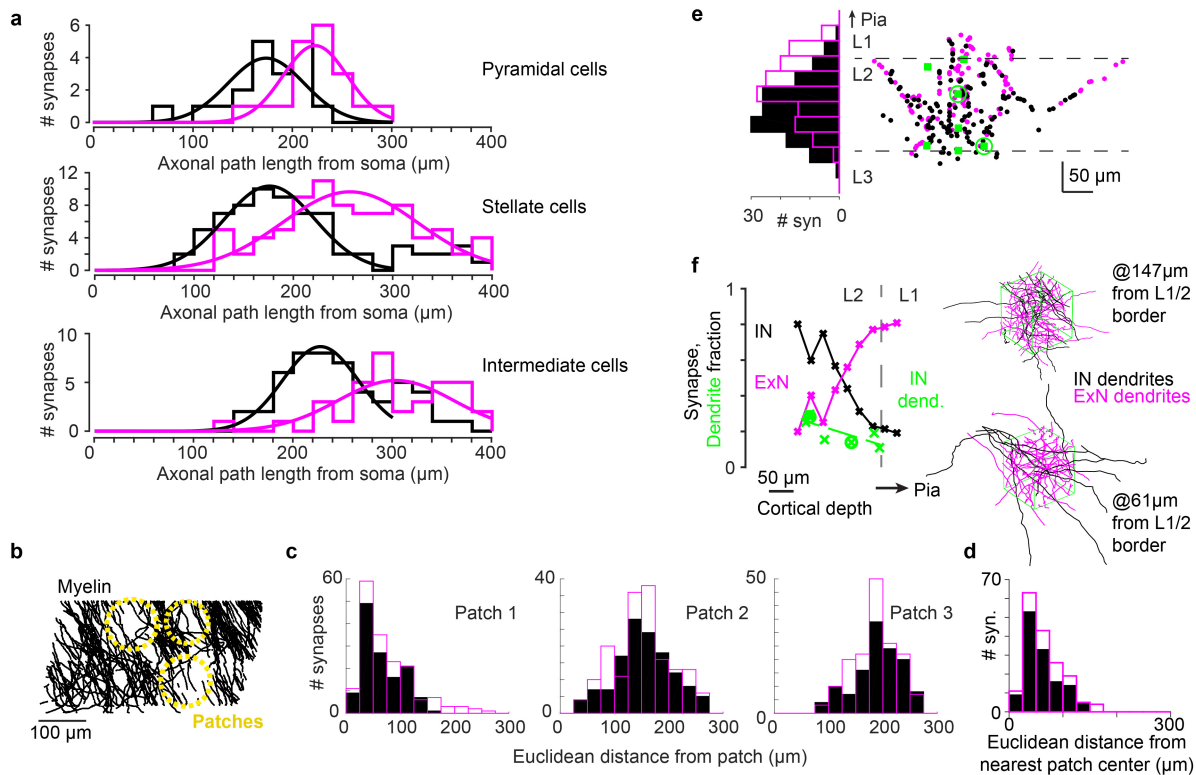
**Extended Data Figure 3 | PLASS with regards to cell types and synapse positions in relation to patches and the cortical axis of the MEC.** See Fig. 2. **a**, Position of output synapses along presynaptic ExN axons analysed separately for consensus pyramidal cells (top; $n = 6$ axons, $n = 19$ (synapses onto excitatory cells) versus $n = 19$ (inhibitory targets), $222 \pm 32 \mu m$ versus $173 \pm 38 \mu m$, mean $\pm$ s.d., $t$-test, Wilcoxon rank-sum test and randomization test, $P < 10^{-3}$), stellate cells (middle; $n = 4$ axons, $n = 36$ (synapses onto excitatory cells) versus $n = 51$ (inhibitory targets), $303 \pm 58 \mu m$ versus $249 \pm 53 \mu m$, mean $\pm$ s.d., $t$-test, Wilcoxon rank-sum test, $P < 10^{-4}$; randomization test, $P < 10^{-3}$) and intermediate types (bottom; $n = 5$ axons, $n = 81$ (synapses onto excitatory cells) versus $n = 70$ (inhibitory targets), $257 \pm 68 \mu m$ versus $202 \pm 75 \mu m$, mean $\pm$ s.d., $t$-test, Wilcoxon rank-sum test, $P < 10^{-5}$; randomization test, $P < 10^{-3}$). Note that all ExNs exhibit PLASS. **b**, Reconstruction of all myelinated axons (black) in L1 and upper L2, projected in the tangential plane. Yellow, circular areas of low myelin density previously identified with the patches of CB$^+$ neurons in the MEC[25]. **c, d**, Distribution of distance of synapses to each of the three patch centres (**c**) and to the nearest patch centre (**d**). Note that no distance bias for interneuron-targeting (black) versus ExN-targeting (magenta) synapses can be seen. **e**, Output synapses along the radial cortex axis (cortical depth, histogram on the left) and in

paracoronal plane of the MEC (right, plane of imaging; see Fig. 1a). The synapse distribution along the cortical depth shows a bias of inhibitory targets towards deeper L2 ($n = 15$ axons, $n = 136$ (synapses onto excitatory cells) versus $n = 140$ (inhibitory targets), $223 \pm 47 \mu m$ versus $189 \pm 45 \mu m$, mean $\pm$ s.d., $t$-test, $P < 10^{-8}$, reported as the relative position to the bottom of the dataset). Green, location of seven cubes with a size of $10 \times 10 \times 10 \mu m^3$ each in which dendrites were densely reconstructed. Green circles, dense reconstructions shown in **f**. **f**, Left, fraction of ExN output synapses made onto dendritic shafts (black) versus spines (magenta) over cortical depth. The fractional path length of smooth dendrites sampled at seven different cortical locations is also shown (green, examples on the right). Note that while the fraction of smooth dendrites is about twofold higher in lower L2 than in upper L2, its gradient cannot account for the about fourfold bias of output synapses onto interneurons in lower L2 (black versus green lines). Green dashed line, linear fit to the interneuron dendrite fraction ($n = 7$, see Methods). Right, skeleton reconstructions of all dendrites within a $10 \times 10 \times 10 \mu m^3$ cube sampled at about $150 \mu m$ (top) and about $60 \mu m$ (bottom) from the L1/2 border. Interneuron dendrites, black; ExN dendrites, magenta. Scale bars, $100 \mu m$ (**b**) and $50 \mu m$ (**e, f**).
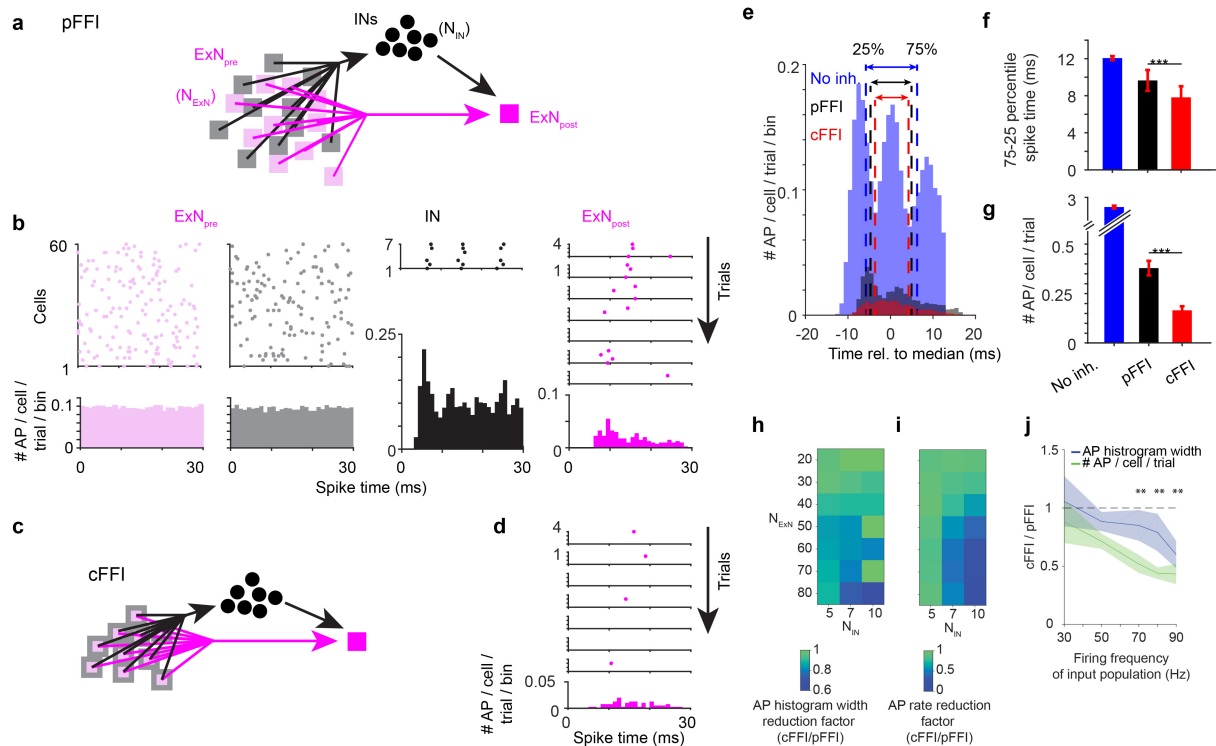
**Extended Data Figure 4 | Functional comparison of population and cellular feedforward inhibition (simulations).** See also Fig. 3. **a**, Sketch of an example circuit converging onto a postsynaptic ExN (magenta square) in population feedforward inhibition (pFFI) comprising a pool of presynaptic ExNs (light magenta) that target the postsynaptic ExN, in parallel to a pool of presynaptic ExNs (grey) from the same presynaptic population that target a pool of interneurons, which in turn converge onto the postsynaptic ExN. Note that in the case of pure pFFI, the two sets of presynaptic neurons are disjunct (light magenta versus grey). **b**, Simulated spike histograms for the presynaptic populations (left), the resulting simulated spike distribution in the interneuron population (single neurons, top; summed histogram over 100 trials, bottom) and the resulting simulated spike distribution in the target ExN (top right, four example cells). Note that the statistics of spiking in presynaptic population are indistinguishable between both presynaptic populations (left). **c**, Sketch of an example circuit configured as cFFI. Note that presynaptic neurons that innervate the postsynaptic ExN are the same ones that innervate the pool of interneurons (as shown in Fig. 3). **d**, Example simulated spike distribution (top, four modelled neurons, six repetitions shown) and average spike histogram per stimulus (bottom) in cFFI configuration. The spike distribution of the presynaptic ExN population is as in **b**, grey panel; and therefore the interneuron spike distribution is as in b, black panel. Note the more narrow distribution and lower spike rate compared to pFFI (**b**). **e**, Average simulated spike histogram of four cells (aligned to median per cell), 2,000 trials each, for the conditions: no inhibition (blue),

pFFI (black), cFFI (red). Arrows indicate width between 25th and 75th percentile. **f, g**, Quantification of cFFI versus pFFI effects on the width of the postsynaptic timing distribution of action potentials (**f**) and the number of action potentials (**g**). Note that cFFI further suppresses the rate of action potentials compared to pFFI (**g**; by twofold, $0.16 \pm 0.02$ (cFFI) versus $0.37 \pm 0.04$ (pFFI) action potentials per cell per trial, mean $\pm$ s.d., $t$-test, ***$P < 10^{-22}$) and narrows the timing of action potentials (**f**; by 1.8 ms, width of spike time histogram $7.8 \pm 1.2$ ms (cFFI) from $9.7 \pm 1.1$ ms under pFFI, mean $\pm$ s.d., $n = 2,000$ trials per cell, $t$-test, ***$P < 10^{-4}$). **h, i**, Stability of the effect of cFFI on spike timing and spike rate under variation of excitatory and inhibitory circuit convergence. **h**, The effect of cFFI on spike timing measured as the decrease in spike histogram width (see **e, f**); relative reduction in 75th-to-25th percentile is reported for cFFI versus pFFI ($P < 0.01$ for $N_{ExN} = 50-80$ and $N_{IN} = 5-7$, $t$-test over 1,000 trials per postsynaptic cell). **i**, Relative reduction in spike rate in cFFI compared to pFFI. Note that the spike rate reduction is most substantial (more than twofold) for presynaptic pool sizes of $N_{ExN} = 60-80$ and $N_{IN} = 7-10$ ($P < 10^{-5}$ for $N_{ExN} = 30-80$ and $N_{IN} = 7-10$; $P < 0.05$ for $N_{IN} = 5$; $t$-test over 1,000 trials per postsynaptic cell). **j**, The effect of presynaptic spike rate on cFFI. Note that for a range of 50–90 Hz presynaptic activity, both the time histogram width and the rate of action potentials are significantly reduced compared to pFFI (**$P < 0.01$ for histogram width of action potentials; $P < 10^{-6}$ for the spike rate of action potentials; one-sided $t$-test against 1). Data are mean $\pm$ s.d. (**f, g**).
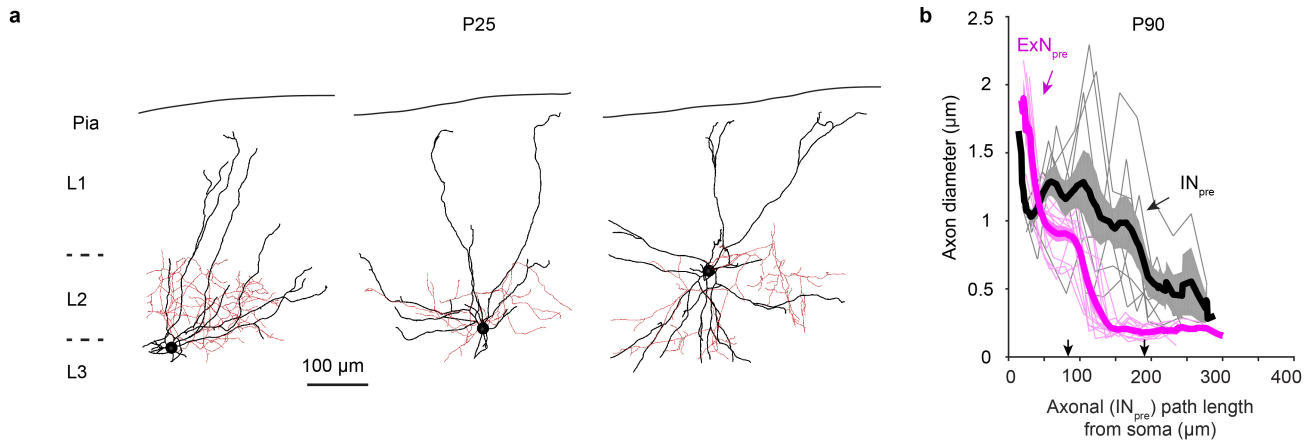
**Extended Data Figure 5 | Axonal architecture of interneurons.**
See Fig. 5. **a**, Morphologies of three interneurons (see Fig. 5b) involved in cFFI circuits. From left to right: 4.5, 2.3 and 3.6 mm reconstructed axonal path length (red), respectively. Scale bar, 100 μm. **b**, Development of axon diameters along the trajectory between soma and distal synapses for one interneuron ($n = 7$ synapses, grey traces) and for three ExNs ($n = 12$ synapses, magenta traces) from the P90 dataset. Mean and s.e.m. at intervals of 25 μm distance are shown (based on linear interpolation between diameter measurement locations, see Methods). Note the about 2.7-fold larger diameter of interneuron axons between about 83 and 188 μm path-length distance (indicated by black arrows, $n = 12$ (excitatory) versus $n = 7$ (inhibitory) paths to synapse, $0.4 \pm 0.1$ μm versus $1.09 \pm 0.46$ μm, mean ± s.d., $t$-test, $P < 10^{-3}$, Wilcoxon rank-sum test, $P < 10^{-4}$).
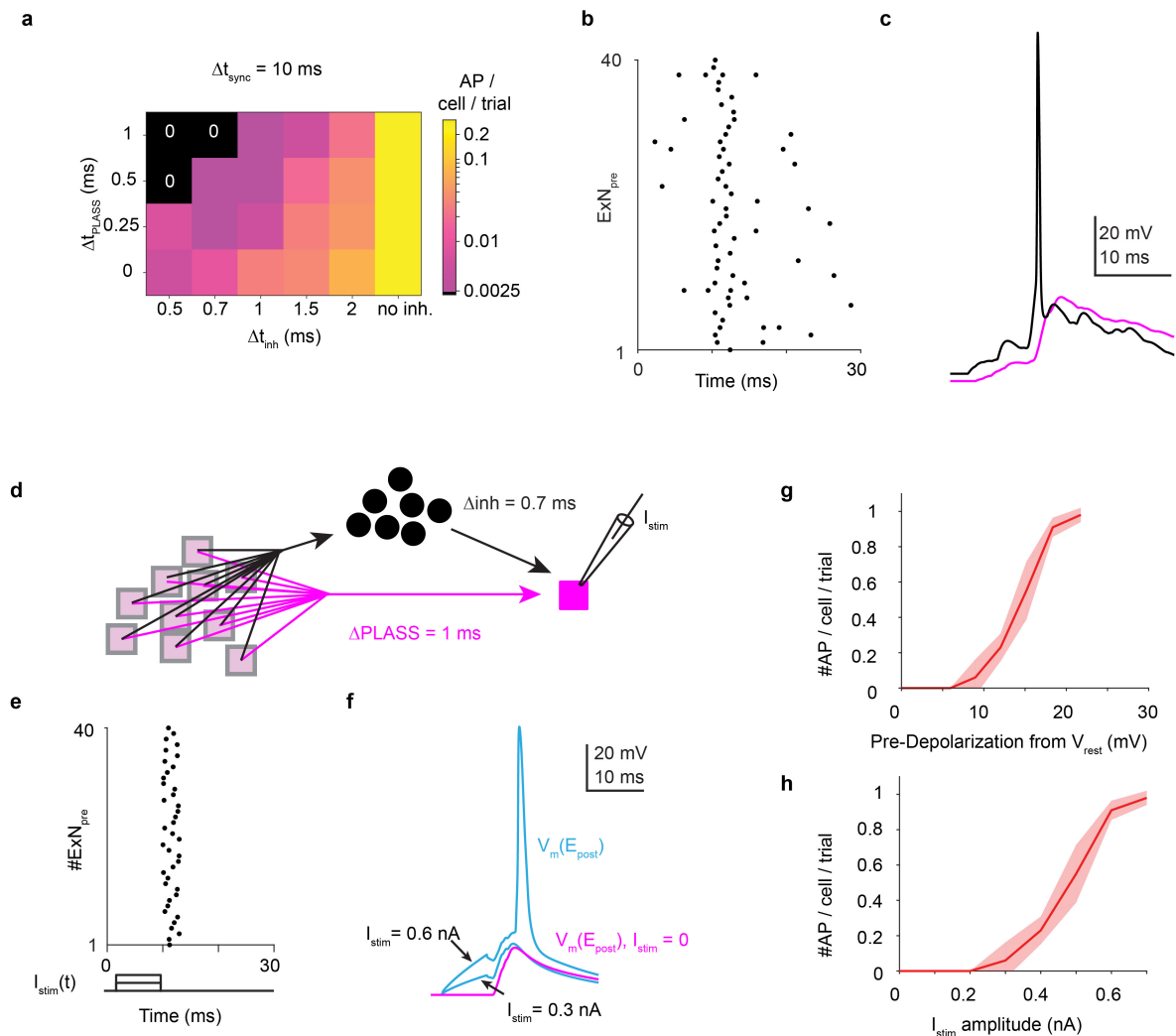
**Extended Data Figure 6 | Numerical simulations of the PLASS–cFFI circuit motif.** See Fig. 6. **a**, The effect of PLASS on suppression of synchronized activity, for a synchronization interval $\Delta t_{sync}$ of 10 ms (compare with Fig. 6g, i). **b**, **c**, The effect of additional background activity on PLASS-based suppression of synchronized activity propagation. Example shows 20 Hz background activity, under which PLASS-based suppression is still effective for synchronization intervals 3 and 10 ms. **d**–**h**, The effect of an additional postsynaptic pre-depolarization on recovery from PLASS-induced supression. **d**, Emulated current injection in the postsynaptic neuron for a PLASS circuit with 0.7 ms inhibitory delay and 1 ms PLASS delay. **e**, Presynaptic synchronized activity and 8-ms-long rectangular pre-depolarizations in the postsynaptic neuron. **f**, Simulated membrane potential transients in the postsynaptic excitatory neuron. Note spike suppression by PLASS (magenta, no additional stimulation), that can be gradually recovered from by current injections of increasing amplitude $I_{stim}$. **g**, **h**, Titration of PLASS recovery over stimulus strength and effective pre-depolarization before the synchronized input activity. A pre-depolarization of 10–20 mV is sufficient for the recovery from PLASS; this could be achieved by underlying membrane potential modulation or an additional gating input to the postsynaptic excitatory neuron, for example at its apical dendrites in L1.

# nature research

Corresponding Author: Moritz Helmstaedter

Date: June 6 2017

# Life Sciences Reporting Summary

Nature Research wishes to improve the reproducibility of the work we publish. This form is published with all life science papers and is intended to promote consistency and transparency in reporting. All life sciences submissions use this form; while some list items might not apply to an individual manuscript, all fields must be completed for clarity.

For further information on the points included in this form, see Reporting Life Sciences Research. For further information on Nature Research policies, including our data availability policy, see Authors & Referees and the Editorial Policy Checklist.

## ▶ Experimental design

1. **Sample size**

   Describe how sample size was determined.

   > Dense reconstruction of one tissue block, replication in a 2nd tissue block.

2. **Data exclusions**

   Describe any data exclusions.

   > no exclusion of data.

3. **Replication**

   Describe whether the experimental findings were reliably reproduced.

   > Replication of experiment and analysis in a 2nd dataset (P25 and P90, Fig. 1-5).

4. **Randomization**

   Describe how samples/organisms/participants were allocated into experimental groups.

   > Dense reconstruction from 2 animals, no group allocation.

5. **Blinding**

   Describe whether the investigators were blinded to group allocation during data collection and/or analysis.

   > n/a

   Note: all studies involving animals and/or human research participants must disclose whether blinding and randomization were used.

6. **Statistical parameters**

   For all figures and tables that use statistical methods, confirm that the following items are present in relevant figure legends (or the Methods section if additional space is needed).

| n/a | Confirmed | |
|---|---|---|
| ☐ | ☒ | The <u>exact</u> sample size (*n*) for each experimental group/condition, given as a discrete number and unit of measurement (animals, litters, cultures, etc.) |
| ☐ | ☒ | A description of how samples were collected, noting whether measurements were taken from distinct samples or whether the same sample was measured repeatedly. |
| ☒ | ☐ | A statement indicating how many times each experiment was replicated |
| ☐ | ☒ | The statistical test(s) used and whether they are one- or two-sided (note: only common tests should be described solely by name; more complex techniques should be described in the Methods section) |
| ☐ | ☒ | A description of any assumptions or corrections, such as an adjustment for multiple comparisons |
| ☐ | ☒ | The test results (e.g. *p* values) given as exact values whenever possible and with confidence intervals noted |
| ☐ | ☒ | A summary of the descriptive statistics, including central tendency (e.g. median, mean) and variation (e.g. standard deviation, interquartile range) |
| ☐ | ☒ | Clearly defined error bars |

*See the web collection on statistics for biologists for further resources and guidance.*

## ▶ Software

Policy information about availability of computer code

7. **Software**

   Describe the software used to analyze the data in this study.

   > Custom MATLAB code for analysis of connectivity data, supplied as SI 2. All

code for numerical simulations is supplied at http://plass.brain.mpg.de (see 'Code availability' section in Methods).

For all studies, we encourage code deposition in a community repository (e.g. GitHub). Authors must make computer code available to editors and reviewers upon request. The *Nature Methods* guidance for providing algorithms and software for publication may be useful for any submission.

## ▶ Materials and reagents

Policy information about availability of materials

### 8. Materials availability

Indicate whether there are restrictions on availability of unique materials or if these materials are only available for distribution by a for-profit company.

no restriction.

### 9. Antibodies

Describe the antibodies used and how they were validated for use in the system under study (i.e. assay and species).

Extended data 1: Calbindin antibody, same as in Ray et al., 2014 Science

### 10. Eukaryotic cell lines

a. State the source of each eukaryotic cell line used.

n/a

b. Describe the method of cell line authentication used.

*Describe the authentication procedures for each cell line used OR declare that none of the cell lines used have been authenticated OR state that no eukaryotic cell lines were used.*

c. Report whether the cell lines were tested for mycoplasma contamination.

*Confirm that all cell lines tested negative for mycoplasma contamination OR describe the results of the testing for mycoplasma contamination OR declare that the cell lines were not tested for mycoplasma contamination OR state that no eukaryotic cell lines were used.*

d. If any of the cell lines used in the paper are listed in the database of commonly misidentified cell lines maintained by ICLAC, provide a scientific rationale for their use.

*Provide a rationale for the use of commonly misidentified cell lines OR state that no commonly misidentified cell lines were used.*

## ▶ Animals and human research participants

Policy information about studies involving animals; when reporting animal research, follow the ARRIVE guidelines

### 11. Description of research animals

Provide details on animals and/or animal-derived materials used in the study.

One P25 and one P90 Chbb:THOM (Wistar) rat (45 g and 235 g, respectively).

Policy information about studies involving human research participants

### 12. Description of human research participants

Describe the covariate-relevant population characteristics of the human research participants.

n/a